# A Dual Phase-Optimized Strategy to Reduce Second-Carrier Harmonic Current for DAB-Based Three-Phase Single-Stage AC–DC Converter

Nan Mo, Qianming Xu, *Member, IEEE*, Jiayu Hu, *Member, IEEE*, Peng Guo, *Member, IEEE*, Guanqing Zhou, Jiayun Liu, Xiangpeng Liu, and An Luo, *Senior Member, IEEE*

***Abstract*—The dual-active-bridge-based three-phase single-stage ac–dc converter has gained significant attention in power conversion applications due to its superior efficiency and compact volume. However, one potential problem is that the dc-side total capacitor ripple current (TCRC) is considerable, which induces capacitor heating and compromises converter reliability. This article presents a Fourier analysis based dual phase-optimized strategy that considers the constraints of phase shift angle (PSA) in DAB converter, aiming to minimize the root mean square (rms) of the lowest frequency harmonic current (LFHC) in TCRC. First, a mathematical model is developed for the single phase (1P) converter, comprising a frequency domain analytical expression of the ripple current and the PSA adjustable range of 1P converter. Subsequently, using the developed model, the initial phase relationships among the three 1P converters are adjusted at the minimum symmetrical interval (30°) of the power grid cycle. Concurrently, the PSA of converters are dynamically optimized at each switching cycle, thereby achieving maximal attenuation of the LFHC. Experimental validation using a 3×1.1-kW prototype demonstrates a 90% reduction in the rms of the LFHC under rated conditions.**

***Index Terms*—Asymmetric operation, dual active bridges (DABs), harmonic elimination, phase shift modulation, signal-stage ac–dc converter.**

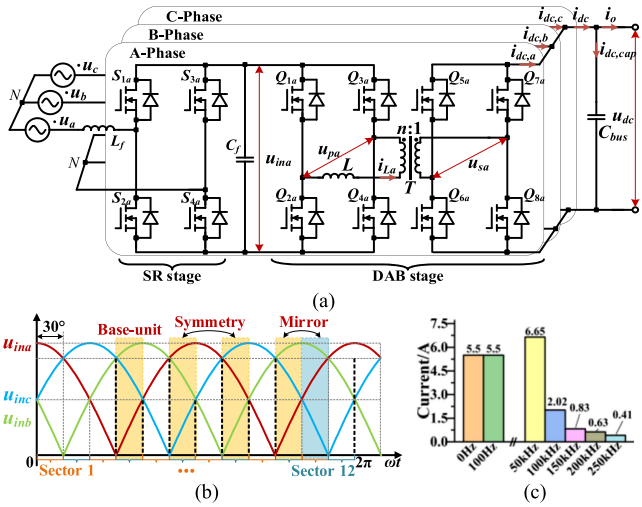


Fig. 1. (a) DAB 3P1S AC–DC converter with star-arrangement of AC ports. (b) Synchronous rectification (SR) bridge output voltage and its periodic characteristics. (c) Fast Fourier transform (FFT) of DC-side output ripple current of single-phase converter at rated output power.

## I. Introduction

IN RECENT years, with the large number of new energy power generation and energy storage systems connected to the grid and the rapid popularity of electric vehicles [1], single-stage isolated ac–dc converters have received widespread attention and research due to their high efficiency and high-power density [2], [3], [4], [5]. Among these, the indirect matrix-type ac–dc converter based on dual active bridge [DAB 3P1S ac–dc converter, as illustrated in Fig. 1(a)] has been the subject of the most extensive research. This is attributable to its simplified power transfer control, facilitated soft-switching [2], and eliminated need for complex commutation strategies [3], [5].

In a DAB-3P1S ac–dc converter system, the dc ports of the three DAB-1P1S ac–dc converters converge on a single point of common coupling (PCC) [6], which is typically referred to as multiphase parallel system (MPS). In this system, the current flowing into the bus capacitor is determined by a combination of the currents flowing into the PCC from the three single-phase (1P) converters and the load current. For a three-phase balanced grid, the ac and dc instantaneous power are balanced in steady state; therefore, the current flowing into the bus capacitor contains solely high-frequency harmonic components. Given that the inductor current within the switching network of a 1P converter is characterized by its purely ac nature and significant fluctuations. The active bridge rectification on the dc side produces a port current with significant ripple, as shown in Fig. 1(c). In the absence of phase control, the harmonic interaction among these 1P converters gives rise to large dc-link ripples current [7]. This phenomenon leads to an elevated root mean square (rms) value of the total capacitor ripple current (TCRC), consequently

Received 15 January 2025; revised 13 April 2025; accepted 24 May 2025. Date of publication 3 June 2025; date of current version 5 August 2025. This work was supported in part by the National Natural Science Foundation of China under Grant 52127901 and Grant 52207198, and in part by the Scientific Research Innovation Capability Support Project for Young Faculty under Grant ZYGXQNJSKYCXNLZCXM-D4. Recommended for publication by Associate Editor M. Amirabadi. *(Corresponding author: Qianming Xu.)*

The authors are with the State Key Laboratory of High-Efficiency and High-Quality Conversion for Electric Power, Hunan University, Changsha 410082, China (e-mail: monan777@hnu.edu.cn; xqm@hnu.edu.cn; hujiayu@hnu.edu.cn; pengguo92@hnu.edu.cn; zhougq1998@hnu.edu.cn; ljy_666@hnu.edu.cn; liuxiangpeng@hnu.edu.cn; an_luo@hnu.edu.cn).

Color versions of one or more figures in this article are available at https://doi.org/10.1109/TPEL.2025.3574380.

Digital Object Identifier 10.1109/TPEL.2025.3574380

escalating the hot spot temperature and curtailing the lifespan of the bus capacitor. Meanwhile, for the three 1P converters, in order to achieve a unity power factor, the instantaneous transfer power of each is not equal. This results in the different ripple current characteristics (both magnitude and phase) of the three parallel 1P converters flowing into the PCC, causing the system to exhibit typical asymmetrical characteristics. Under such conditions, the uniform phase-shift technique (UPST), which mandates 360°/N phase intervals among N parallel modules per switching cycle, fails to optimally minimize the TCRC [7]. Hence, this study focuses on the optimal phase configuration of three 1P converters to minimize the rms of TCRC.

In [8], [9], [10], and [11], researchers reduced the dc-link ripple current in three-phase six-switch buck-type rectifiers through optimized switching vector sequences. Song et al. [12] achieved the reduction of both dc-side ripple current and grid current total harmonic distortion (THD) in high-frequency-link matrix converters by simultaneously optimizing vector sequences and their time durations. Moreover, to optimize the intermediate dc-link ripple current in two-stage ac–dc converters, Mallik and Khaligh [13] concentrated on reducing the ripple current of the front-end power factor correction stage by optimizing modulation, whereas Alcaide et al. [14] concentrated on reducing the ripple current of the back-end dc–dc stage by changing the inter-leg phase shift angle (PSA). It should be noted that the aforementioned methods are specifically designed for single converter, which is different from the MPS discussed in this article.

In [15] and [16], the dc bus capacitor ripple current is reduced for the back-to-back converters by coordinating the switching behavior of the two parallel converters. Tcai et al. [15] propose a novel discontinuous pulsewidth modulation strategy that manipulates the clamping states of the two parallel converters to reduce dc-link current ripple. Xue et al. [16] developed a model predictive control approach that directly generates switching pulses without carrier wave. This approach generates a distinctive ripple current spectrum compared to that of space-vector modulation, thus facilitating enhanced inter-converter ripple current cancellation. Tong et al. [17] determined the optimal vector action times for minimizing dc-side ripple current in parallel three-phase inverter system. Furthermore, the study identified an optimal vector sequences while considering the circulating current. Nevertheless, the modulation discussed in these references are not applicable for the topology used in our study. Wang et al. [18], [19], [20] present a cooperative control strategy for parallel converters in more-electric aircraft dc generation systems to reduce dc-link ripple currents. However, for the DAB 1P1S ac–dc converter, the ripple current spectrum throughout the grid cycle exhibits substantial complexity. We can only extract switching-cycle-scale frequency-domain expressions, thereby limiting application of the aforementioned methods to this topology.

In multidrive systems, dc bus ripple current generated by the parallel inverter were maximally canceled out each other with the optimal phase shifts of the modulation and carrier signals [21], [22]. Poon et al. [23] investigated the application of carrier-based optimized phase shift modulation in distributed generation system, aiming to enhance the power quality of the output ac current. Zhang et al. [24] investigated the impact of carrier interleaving techniques on dc-link ripple current in parallel-connected three-phase rectifier systems. However, the aforementioned studies utilize a fixed PSA throughout the entire fundamental period during steady state. Consequently, the rms value of ripple current obtained by interleaving the parallel inverter may not be optimal.

Schuck and Pilawa-Podgurski [25] and An et al. [26] employ phasor synthesis techniques to rapidly determine intermodule optimal phase shift angle (OPSA) for targeted harmonic cancellation in parallel/series-connected systems. Notably, a simplified computational method for systems with more than three submodules is proposed in [26]. However, it must be emphasized that these studies primarily focus on nonisolated converters. In contrast, this work investigates dc-side ripple current optimization in isolated converter, where the phase of the switching network cannot be adjusted arbitrarily [28].

To the best of our knowledge, only a limited number of studies, such as [7] and [27], have specifically investigated dc-side ripple current optimization in DAB converters. However, both [7] and [27] focus exclusively on dc–dc systems where OPSA typically remain constant under steady-state conditions, leading researchers to overlook the isolated converters' limited phase regulation capability. By contrast, the DAB 3P1S ac–dc converter is characterized by the alteration of the harmonic characteristics of the three 1P converters per switching cycle, even under steady-state conditions. This results in a continuous adjustment of the OPSA. In this instance, the fact that the restricted PSA adjustable range cannot be disregarded. It must be considered when determining the OPSA; otherwise, severe dc bias currents will be generated [28].

In light of the constraint on the PSA adjustable range, this study introduces a dual phase-optimized strategy that combines offline optimization of the initial phase relationship with online calculation of the OPSA to effectively eliminate the lowest frequency harmonic current (LFHC) from the TCRC. The main contributions of this article to the field can be summarized as follows.

1) This article highlights the constrained PSA adjustable range in the ripple current optimization of the DAB-3P1S ac–dc converter. This critical limiting factor has been consistently neglected in extant ripple optimization research.
2) A method for calculating the OPSA is presented aimed at minimizing the LFHC, taking into account the constraints on the adjustable range of the PSA. In contrast to the conventional method based on phasor synthesis, the proposed method provides a general solution. Compared with existing methods, the proposed method can prevent the generation of dc bias current in inductors while effectively reducing the rms value of TCRC.

The rest of this article is organized as follows. First, in Section II, the operating characteristics of the DAB-1S ac–dc convertor are analyzed. Furthermore, the time and frequency domain expressions for the dc-link capacitor ripple current are derived. Section III presents an analysis of the adjustable

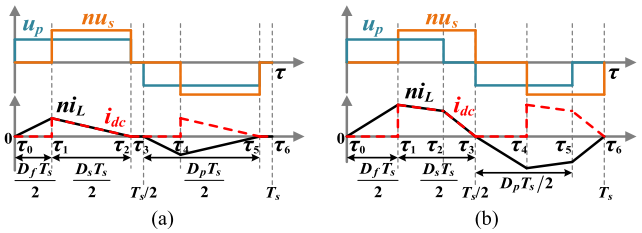


Fig. 2. Key operation waveforms of the decoupled inductor current modulation in the boost condition. (a) TDCM, light-load condition. (b) TCCM, heavy-load condition.

range of PSA, illustrating the limitations of existing OPSA calculation methods. Concurrently, it offers a general solution for the OPSA within the limitations imposed by the constrained PSA adjustable range. This solution is subsequently employed to develop an optimization algorithm, which is utilized to ascertain the optimal initial phase relationship among parallel converters. Section IV experimentally verifies the effectiveness of the proposed method. Finally, Section V provides a summary of this article.

## II. Mathematical Description of the Ripple Current Superposition

### A. Power Circuit Topology and Modulation Strategy

The configuration of the DAB 3P1S ac–dc converter is illustrated in Fig. 1. It includes three identical 1P converters paralleled on the dc side. Each converter includes a SR bridge and a DAB dc–dc converter. Since the hardware parameters and the modulation strategy are identical for all three, only A-phase converter is used as an illustrative example. The primary side of the DAB is a full bridge consisting of switches $Q_{1a}$–$Q_{4a}$, and the secondary side is also a full bridge composed of switches $Q_{5a}$–$Q_{8a}$. The inductor $L_f$ and capacitor $C_f$ form a low-pass filter. $u_a$ is the grid voltage connected to the A-phase converter. $u_{\mathrm{ina}}$ is the rectified voltage of $u_a$. $i_{La}$ is the current of inductor $L$ and $i_{\mathrm{dc},a}$ is the dc side port current of A-phase converter. $C_{\mathrm{bus}}$ is the dc-link capacitor used to maintain dc voltage stability and absorb ripple current. $n$ denotes the transformer turns ratio.

The typical waveforms of the 1P converter are shown in Fig. 2, known as decoupled inductor current modulation, and were proposed by Li [4]. This modulation method has been demonstrated to yield a lower current THD than optimal peak current modulation [29] under the same condition [2]. Therefore, this method is selected to verify the effectiveness of the proposed harmonic current elimination method in Section III. As this harmonic current elimination method does not affect the calculation of the control variables ($D_p$, $D_s$, and $D_f$, whose definitions are marked in Fig. 2) related to transfer power, and given the length of this article, the results are given directly in Table I. Where $G = u_{\mathrm{ina}}/nu_{\mathrm{dc}}$ is the voltage transfer ratio. $P_t$ is the instantaneous transfer power.

TABLE I
Calculation Expression of Phase-Shift Ratios

| Mode | Power range | Control variables |
|---|---|---|
| $G<1$, $P_n=\frac{8f_sLP_t}{nu_{\mathrm{dc}}u_{\mathrm{ina}}}$ | $P_n\in[0,2G(1-G)]$ | $\begin{cases}D_p=\sqrt{P_n/[2G(1-G)]}\\ D_s=GD_p, D_f=D_p-D_s\end{cases}$ |
| | $P_n\in\left(2G(1-G),\frac{2G}{G^2+G+1}\right]$ | $\begin{cases}D_p=\frac{1+G+\sqrt{G-P_n\left(1+G+G^2\right)/2}}{1+G+G^2}\\ D_s=GD_p, D_f=1-D_s\end{cases}$ |
| $G>1$, $P_n=\frac{8f_sLP_t}{nu_{\mathrm{dc}}u_{\mathrm{ina}}}$ | $P_n\in\left[0,\frac{2(G-1)}{G^2}\right]$ | $\begin{cases}D_p=\sqrt{P_n/(2G-2)}\\ D_s=GD_p, D_f=0\end{cases}$ |
| | $P_n\in\left[\frac{2(G-1)}{G^2},\frac{2G}{G^2+G+1}\right)$ | $\begin{cases}D_p=\frac{1+G+\sqrt{G-P_n\left(1+G+G^2\right)/2}}{1+G+G^2}\\ D_s=GD_p, D_f=1-D_s\end{cases}$ |

### B. Mathematical Model of DAB 3P1S AC–DC Converter

In order to analyze the output ripple current of the dc port, it is first necessary to analyze the current of the switching network. According to Fig. 2, the inductor current can be expressed as (1). Taking trapezoidal continuous conduction mode (TCCM) as an example, in steady state, the essential waveform of DAB is shown in Fig. 2(b). The A-phase converter is utilized as a demonstrative exemplar. The inductor current during any switching cycle can then be expressed as (2), where $i_{\mathrm{La}}(\tau_0,t)=-i_{\mathrm{La}}(\tau_3,t)=0$, $i_{\mathrm{La}}(\tau_1,t)=-i_{\mathrm{La}}(\tau_4,t)=u_{\mathrm{ina}}(t)D_fT_s/2L$, $i_{\mathrm{La}}(\tau_2,t)=-i_{\mathrm{La}}(\tau_5,t)=nu_{\mathrm{dc}}(t)(1\text{-}D_p)T_s/2L$. "$t$" refers to the time in an ac line cycle (50 Hz), while "$\tau$" refers to the time in one switching cycle (25 kHz in the experimental prototype).

$$L\cdot di_{\mathrm{La}}/d\tau = u_{\mathrm{pa}}-nu_{\mathrm{sa}} \tag{1}$$

$$i_{\mathrm{La}}(\tau,t)=\begin{cases}\frac{u_{\mathrm{ina}}(t)}{L}\tau+i_{La}(\tau_0,t) & ,\tau\in[\tau_0,\tau_1]\\ \frac{u_{\mathrm{ina}}(t)-nu_{\mathrm{dc}}}{L}(\tau-\tau_1)+i_{\mathrm{La}}(\tau_1,t) & ,\tau\in(\tau_1,\tau_2]\\ \frac{-nu_{\mathrm{dc}}}{L}(\tau-\tau_2)+i_{\mathrm{La}}(\tau_2,t) & ,\tau\in(\tau_2,\tau_3]\\ -i_{\mathrm{La}}(\tau-\frac{T_s}{2},t) & ,\tau\in(\tau_3,\tau_6]\end{cases} \tag{2}$$

$$i_{\mathrm{dc},a}(\tau,t)=n\cdot\begin{cases}0 & ,\tau\in[\tau_0,\tau_1]\\ \frac{-nu_{\mathrm{dc}}}{L}(\tau-\tau_1)+i_{\mathrm{La}}(\tau_1,t) & ,\tau\in(\tau_1,\tau_2]\\ 0 & ,\tau\in(\tau_2,\tau_3]\end{cases} \tag{3a}$$

$$i_{\mathrm{dc},a}(\tau,t) = n\cdot\begin{cases}0 & ,\tau\in[\tau_0,\tau_1]\\ \frac{u_{\mathrm{ina}}(t)-nu_{\mathrm{dc}}}{L}(\tau-\tau_1)+i_{\mathrm{La}}(\tau_1,t) & ,\tau\in(\tau_1,\tau_2]\\ \frac{-nu_{\mathrm{dc}}}{L}(\tau-\tau_2)+i_{\mathrm{La}}(\tau_2,t) & ,\tau\in(\tau_2,\tau_3]\end{cases}. \tag{3b}$$

As illustrated in Fig. 2, in one switching cycle, when $\tau_0<\tau<\tau_1$, $i_{\mathrm{dc},a}=0$, and when $\tau_1<\tau<\tau_3$, $i_{\mathrm{dc},a}=ni_{\mathrm{La}}$, the first half cycle ($\tau_0<\tau<\tau_3$) and the second half cycle ($\tau_3<\tau<\tau_6$) of $i_{\mathrm{dc},a}$ are the same. This indicates that the fundamental frequency of the DAB dc port output current is twice that of the switching frequency. Consequently, $i_{\mathrm{dc},a}$ can be represented by the first half switching cycle, as shown in (3b). Similarly, in triangular discontinuous conduction mode (TDCM), the dc port output current can be expressed as (3a). Then, the DAB stage is

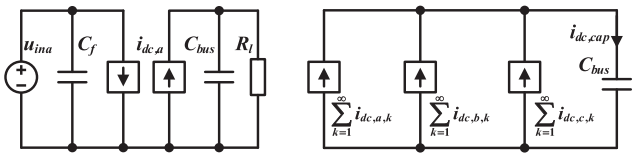


Fig. 3. (a) Large-signal diagram of the DAB reduced-order model. (b) Harmonic equivalent circuit of the DC side of DAB 3P1S AC–DC converter.

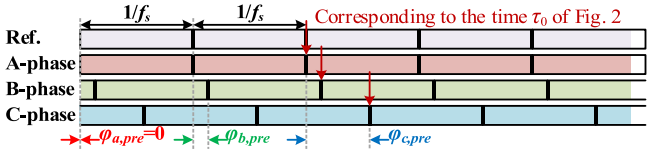


Fig. 4. Initial phase relationships for three 1P converters in the 0°–30° of grid.

simplified to a first-order system, as shown in Fig. 3(a)

$$\begin{cases} i_{\mathrm{dc},a}(\tau,t) = \frac{A_{a,0}}{2} + \sum_{k=1}^{\infty} A_{a,k}\cos\left(2k\omega_s\tau + k\varphi_{a,0} + \varphi_{a,k}\right) \\ A_{a,0} = a_{a,0} = 4f_s\int_0^{T_s/2} i_{\mathrm{dc},a}(\tau,t)\,d\tau \\ a_{a,k} = 4f_s\int_0^{T_s/2} i_{\mathrm{dc},a}(\tau,t)\cos\left(2k\omega_s\tau\right)d\tau \\ b_{a,k} = 4f_s\int_0^{T_s/2} i_{\mathrm{dc},a}(\tau,t)\sin\left(2k\omega_s\tau\right)d\tau \\ A_{a,k} = \sqrt{a_{a,k}^2 + b_{a,k}^2},\ \varphi_{a,k} = -\mathrm{atan2}[b_{a,k}, a_{a,k}] \in (-\pi,\pi] \\ \omega_s = 2\pi f_s,\ T_s = 1/f_s \end{cases} \tag{4}$$

Considering a cycle ($\tau_0 < \tau < \tau_3$), according to the Fourier transform theory, $i_{dc,a}$ can be decomposed by trigonometric series, where twice the switching frequency is the fundamental frequency for Fourier expansion, and it can be expressed as (4), where $k = 1, 2, \ldots$ denotes the harmonic components of different orders, $f_s$ denotes the switching frequency, atan2 is the inverse tangent function that returns the angle in the interval of $(-\pi, \pi]$. The phase angle of the $k$th harmonic is given by the sum of $k\varphi_{a,0}$ and $\varphi_{a,k}$. $\varphi_{a,k}$ is determined by the operating conditions and it remains constant for any given switching period. $\varphi_{a,0}$ is determined by the phase of $i_{\mathrm{dc},a}$, which is the sole available control degree of freedom to optimize the TCRC. This parameter can be modified in two distinct ways: first, by modifying the phase shift within the switching cycles of the 1P converter, referred to as $\varphi_{a,\mathrm{int}}$. Since the adjustment of this parameter affects the initial value of the inductor current during the switching cycle, its adjustable range is limited, which will be analyzed in detail in Section III; and second, by altering the initial phase relationship among the three 1P converters, denoted as $\varphi_{a,\ \mathrm{pre}}$. In the present analysis, the $\varphi_{x,\ \mathrm{pre}}$ ($x = a, b, c$) is implemented by maintaining a fixed phase for the A-phase converter while varying the phases of the B-phase and C-phase converter. That is to say, $\varphi_{a,\ \mathrm{pre}}$ is equivalent to zero, as shown in Fig. 4. Therefore, $\varphi_{a,0}$ can be represented as the sum of $\varphi_{a,\mathrm{pre}}$ and $\varphi_{a,\mathrm{pre}}$. Furthermore, given the symmetry of the three-phase grid voltage, a grid cycle was divided into 12 sectors, as illustrated in Fig. 1(b). The values of $\varphi_{b,\mathrm{pre}}$ and $\varphi_{c,\mathrm{pre}}$ are constant within a sector and are modified solely at the time of sector switching. The subsequent section will analyze the calculation method of $\varphi_{x,0}$ ($x = a, b, c$) in detail.

By substituting (3a) and (3b) into (4), the Fourier coefficients of the 1P converter' output ripple currents can be deduced for each of the two modes. To simplify the analysis, these coefficients can be normalized using $I_b = n^2 u_{\mathrm{dc}}/4\pi^2 f_s L$, as delineated in (5a) and (5b). Utilizing the aforementioned method, the Fourier coefficients for the TCCM and TDCM under buck conditions are also obtained, as demonstrated in (5b) and (5c), respectively. It should be noted that $k = 0$ indicates the dc component of the output current, while this item indicates the average output current of the current switching cycle, which is positively related to the transfer power. Furthermore, $k > 0$ indicates the harmonic components of the output current. It is assumed that these portions of the current are completely absorbed by the dc-link capacitor due to the fact that the capacitor's high-frequency impedance is considerably smaller than that of the load. Given that the 3P converter's ac- and dc-instantaneous transfer power is in equilibrium, $a_{a,0} + a_{b,0} + a_{c,0} = i_o$ can be established. When focusing solely on the harmonic components of the output current, it is possible to derive the harmonic equivalent circuit for the dc port of the DAB 3P1S ac–dc converter by utilizing the reduced-order model of the 1P converter, as depicted in Fig. 3(b). Prior research has demonstrated that the LFHC is the predominant component of TCRC [7]. This conclusion can also be verified from Fig. 1(c). In addition, the equivalent series resistance (ESR) of the electrolytic capacitor exhibits a negative correlation with the frequency of the harmonic current [30], indicating that the LFHC contributes most significantly to bus capacitor heating. Moreover, for MPS comprising a maximum of three modules, only a single frequency of harmonic current can be optimal eliminated [25]. Therefore, harmonic elimination in the following focuses only on the LFHC, that is to say, $k = 1$. Then, following simplification, the TCRC can be expressed as the sum of three sinusoidal functions with varying amplitudes and phases, as shown in (6)

$$\begin{cases} a_0 = \pi^2 d D_f D_s \\ a_k = (1-G)\begin{bmatrix}\cos(2\pi k D_f) - 2\pi k D_s \sin(2\pi k D_f) \\ -\cos(2\pi k D_p)\end{bmatrix}\Big/ k^2 \\ b_k = (1-G)\begin{bmatrix}2\pi k D_s \cos(2\pi k D_f) - \sin(2\pi k D_p) \\ +\sin(2\pi k D_f)\end{bmatrix}\Big/ k^2 \end{cases} \tag{5a}$$

$$\begin{cases} a_0 = \left[(1-D_p)D_s + G D_f (D_p - D_f)\right]\pi^2 \\ a_k = \begin{bmatrix}(1-G)\cos(2\pi k D_f) + G\cos(2\pi k D_p) \\ -2\pi k G D_f \sin(2\pi k D_f) - 1\end{bmatrix}\Big/ k^2 \\ b_k = \begin{bmatrix}2\pi k G D_f \cos(2\pi k D_f) \\ +(1-G)\sin(2\pi k D_f) + G\sin(2\pi k D_p)\end{bmatrix}\Big/ k^2 \end{cases} \tag{5b}$$

$$\begin{cases} a_0 = \pi^2\left(D_s^2 - D_s D_p\right) \\ a_k = \left[G\cos(2\pi k D_p) - \cos(2\pi k D_s) + 1 - G\right]/k^2 \\ b_k = \left[G\sin(2\pi k D_p) - \sin(2\pi k D_s)\right]/k^2 \end{cases} \tag{5c}$$

$$i_{\mathrm{dc,cap},1}(t,\tau) = i_{\mathrm{dc},a,1}(t,\tau) + i_{\mathrm{dc},b,1}(t,\tau) + i_{\mathrm{dc},c,1}(t,\tau). \tag{6}$$

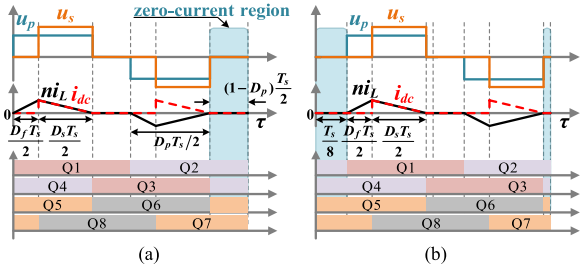


Fig. 5. (a) Voltage-current waveforms for TDCM without phase shift. (b) Voltage-current waveforms for TDCM phase-shifted to the right by $T_s/8$.

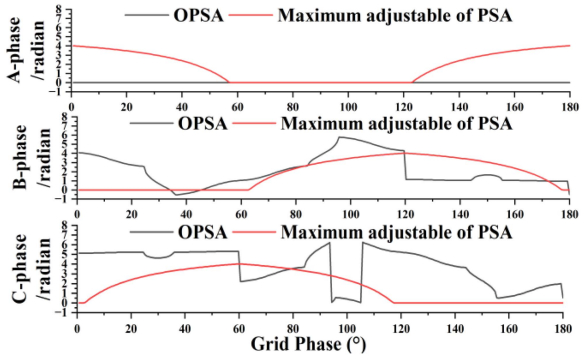


Fig. 6. OPSA of three 1P converters to obtain the minimum LFHC and the maximum adjustable PSA per switching cycle. $\varphi_{x,\mathrm{pre}} = 0$ ($x = a, b, c$), $u_{\mathrm{dc}} = 300$V, $u_{\mathrm{ac}} = 110$ Vrms, $f_s = 25$ kHz, $n = 0.5$, and $L = 40$ $\mu$H, the load rate is 50%.

Given that the three summation terms in (6) are sinusoidal functions with the same frequency, circuit theory dictates that these functions' summation relationship can be represented by phasor resultant. By representing each term of (6) in plural form ($\dot{A}_{x,1} \overset{\mathrm{def}}{=} A_{x,1}\mathrm{e}^{\mathrm{j}(\varphi_{x,0}+\varphi_{x,1})} = A_{x,1}\mathrm{e}^{\mathrm{j}\phi_x}, x = a, b, c$), (6) can be equivalently rewritten as (7). Where $\phi_x$ denotes the argument angle of the phasor. Subsequently, the objective of minimizing the LFHC can be expressed by minimizing the modulus of the phasor sum in complex plane

$$A_{\mathrm{cap},1}e^{\mathrm{j}\phi_{\mathrm{cap}}} = A_{a,1}e^{\mathrm{j}\phi_a} + A_{b,1}e^{\mathrm{j}\phi_b} + A_{c,1}e^{\mathrm{j}\phi_c}. \tag{7}$$

## III. Dual Phase-Optimized Strategy

First, an expression for the adjustable range of the PSA is provided based on the operating characteristics of the DAB-based converter. This expression is then compared with the OPSA calculated under a given operating condition. This comparison serves to illustrate the imperative of deliberating on the adjustable range of PSA. Subsequently, a detailed computational description of the method proposed in this article is provided.

### A. Adjustable Range of PSA

In DAB converters, the adjustment of ripple current's phase is accomplished by modifying the phases of the voltage in the switching network and the inductor current. However, it is imperative to note that the generation of dc bias current on the inductor during the operation of a DAB-based converter must be prevented. This can be achieved by ensuring that the initial currents of all switching cycles are identical [4]; specifically, for decoupled inductor current modulation, the initial current of each switching cycle must be set to zero. As illustrated in Fig. 5(a), when the converter operates in TDCM, the inductor current remains at zero during the intervals $[D_pT_s/2,\ T_s/2]$ and $[(1+D_p)T_s/2,\ T_s]$, which are designated as zero-current regions (ZCRs). It is evident that when a phase shift operation is performed on the TDCM, one can guarantee initial current constraint satisfaction by positioning the initial point of the switching cycle within the ZCR. As illustrated in Fig. 5, the waveform before and after phase shift operation in TDCM are presented for comparison. It can be observed that the initial current is zero both before and after phase shift operation. As $D_p$ is greater than zero, the width of the ZCR is less than $T_s/2$, which consequently implies that the adjustable range of PSA in this mode must be less than $2\pi$, as given by (8a). Similarly, for TCCM, the inductor current is zero at only a few time points, namely, $\tau = \{0,\ T_s/2,\ T_s\}$, indicating that the ZCR in TCCM is nonexistent and that TCCM lacks the capability for PSA adjustment, as shown in (8b). It should be noted that a rightward displacement of the current waveform within the time domain signifies a clockwise rotation of the phasor in the complex plane, resulting in a reduction of its argument angle. Hence, the adjustable range of the argument angle of each phasor can be expressed as (9)

$$\varphi_{x,\mathrm{int}} \in [0, 2\pi(1 - D_{p,x})], x = a, b, c \tag{8a}$$

$$\varphi_{x,\mathrm{int}} \in \{0\}, x = a, b, c \tag{8b}$$

$$\begin{cases} \phi_x \in [\varphi_{x,1}+\varphi_{x,\mathrm{pre}} - \varphi_{x,\mathrm{int,max}},\quad \varphi_{x,1}+\varphi_{x,\mathrm{pre}}], x=a,b,c \\ \varphi_{x,\mathrm{int,max}} = \begin{cases} 2\pi(1-D_{p,x}) & ,\mathrm{TDCM} \\ 0 & ,\mathrm{TCCM} \end{cases}, \varphi_{x,\mathrm{int,min}} = 0 \end{cases}. \tag{9}$$

The preceding analysis demonstrates that a salient attribute of DAB 3P1S ac–dc converters is their constrained adjustable range of PSA (or argument angle of phasor). Therefore, the calculated OPSA must be checked to ensure that it lies within the adjustable range. As illustrated in Fig. 6, the OPSAs of the three 1P converters are presented alongside the maximum PSA of each converter under the corresponding operating conditions. These values are calculated using the method proposed in literature [25] and Eq. (9) in this article, respectively. Given that the phase shift is executed with the A-phase converter acting as a reference, it is unnecessary to account for the phase shift operation of the A-phase converter. In the case of the B-phase converter, which operates in TCCM within the 0°–60° range of the grid cycle, there is an absence of phase adjustment capability during this interval. As a result, the value represented by the red line in the central portion of Fig. 6 is zero within this range. To achieve optimal elimination of the LFHC, the calculated OPSA is depicted as the black line in the figure. It is evident that the OPSA fluctuates continuously and significantly within this interval, surpassing the red line and indicating that the OPSA exceeds the adjustable range of the PSA. A similar phenomenon is observable in the B-phase and C-phase converters during the 60°–180° grid cycle.

### B. Minimum Phasor Sum Under PSA Constraint

To ascertain the minimum phasor sum for the scenario in which the adjustable range of PSA is constrained, the modulus expression for the phasor sum is derived in the complex plane utilizing the projection of the phasors onto the coordinate axes, as shown in (10). For any specified switching period, the moduli of $\dot{A}_{a,1}$, $\dot{A}_{b,1}$, and $\dot{A}_{c,1}$ remain constant. Consequently, the modulus expression as a ternary function that is solely dependent on the argument angle. The feasible region of variables is given in (9). Moreover, given that the modulus of phasor is always non-negative, the objective of identifying the minimum value of the function $f(\phi_a, \phi_b, \phi_c)$ within the feasible region can be simplified as that of determining the minimum value of the function $g(\phi_a, \phi_b, \phi_c) = [f(\phi_a, \phi_b, \phi_c)]^2$ within the same feasible region

$$f(\phi_a, \phi_b, \phi_c) = \sqrt{\left[\sum\nolimits_{x=a,b,c} A_{x,1}\cos(\phi_x)\right]^2 + \left[\sum\nolimits_{x=a,b,c} A_{x,1}\sin(\phi_x)\right]^2}. \tag{10}$$

In accordance with the preceding analysis, each 1P converter exhibits two distinct operational modes, corresponding to two separate adjustable ranges for the PSA. Depending on the number of converters operating in TDCM (or TCCM), the feasible region of the independent variable of $g(\phi_a, \phi_b, \phi_c)$ can be divided into four possible scenarios. These four scenarios will alternate as the grid phase, output average power and output voltage are varied. The following four scenarios will be analyzed individually.

1) *Three 1P Converters Operate in TCCM*: In this scenario, the PSAs of all three 1P converters are not adjustable, and all three variables of function $g(\phi_a, \phi_b, \phi_c)$ are constant values, as shown in (11). Consequently, this precludes any further reduction of the phasor sum. The OPSAs for the three 1P converters in this scenario are shown in (12)

$$\phi_x = \mathrm{fmod}\left[\varphi_{x,1} + \varphi_{x,\mathrm{pre}}, \pi\right], x = a, b, c \tag{11}$$

$$\varphi_{a,\mathrm{int}} = \varphi_{b,\mathrm{int}} = \varphi_{c,\mathrm{int}} = 0. \tag{12}$$

2) *Two 1P Converters Operate in TCCM*: In this scenario, the PSA of the converter operating in TDCM is the only adjustable variable; consequently, two of the three independent variables of the function $g(\phi_a, \phi_b, \phi_c)$ are constant. The analysis is conducted with the A-phase converter operating in TDCM as the basis for investigation. The same conclusions will be obtained by analyzing using two other 1P converters; therefore, they will not be repeated here. In this context, the variables $\phi_b$ and $\phi_c$ are held constant, thus rendering $g(\phi_a, \phi_b, \phi_c)$ a unary function about $\phi_a$. The feasible region of the independent variable of the function $g(\phi_a)$ is shown in (13). The derivative of this function with respect to $\phi_a$ can be derivedin (14), which can subsequently be reformulated as (15) shown at the bottom of the next page, where $A_{\mathrm{sum}}$ and $\phi_{\mathrm{sum}}$ represent the modulus and argument angle of the phasor sum of $\dot{A}_{b,1}$ and $\dot{A}_{c,1}$, respectively. If $A_{\mathrm{sum}}$ is equal to zero, then $g_1'(\phi_a)$ is always equal to zero, and adjusting $\phi_a$ will not affect the value of $g(\phi_a, \phi_b, \phi_c)$. Thus, $\phi_a$ can take any value within its feasible region. To streamline the phase shift operation, the value of $\varphi_{a,\mathrm{int}}$ is set to zero

$$\begin{cases} \phi_a \in [\phi_{a,\min}, \phi_{a,\max}], \\ \phi_{a,\max} = \mathrm{farg}(\varphi_{a,1} + \varphi_{a,\mathrm{pre}}) \\ \phi_{a,\min} = \mathrm{farg}(\varphi_{a,1} + \varphi_{a,\mathrm{pre}} - 2\pi(1 - D_{p,a})) \end{cases} \tag{13}$$

$$g_1'(\phi_a) = 2A_{a,1}\left[A_{b,1}\sin(\phi_b - \phi_a) - A_{c,1}\sin(\phi_a - \phi_c)\right] \tag{14}$$

$$g_{11}''(\phi_a) = -2A_{a,1}A_{\mathrm{sum}}\cos(\phi_{\mathrm{sum}} - \phi_a). \tag{16}$$

Conversely, when $A_{\mathrm{sum}}$ is not equal to zero, by setting $g_1'(\phi_a)$ to zero and ensuring that (16) is greater than zero, it can be demonstrated that the function attains minimal value at $\phi_a = \mathrm{farg}\,(\pi + \phi_{\mathrm{sum}})$, where farg is a custom function that returns the principal argument angle of the input angle in the interval $(-\pi, \pi]$. If this value falls within the feasible region, then this value is deemed to be the OPSA of A-phase converter that minimizes the LFHC. Conversely, in the event that this value falls outside of the feasible region, the two boundary values of the feasible region can be substituted into $g(\phi_a, \phi_b, \phi_c)$. The PSA between the two that results in the smaller value of $g(\phi_a, \phi_b, \phi_c)$ is the OPSA to be sought.

Summarizing the foregoing analysis, the OPSAs for the three 1P converters in this scenario are provided in Table II.

TABLE II
OPSA WHEN TWO 1P CONVERTERS OPERATE IN TCCM

| Condition | OPSA of three 1P converters |
|---|---|
| $A_{\mathrm{sum}} = 0$; | $\varphi_{a,\mathrm{int}} = \varphi_{b,\mathrm{int}} = \varphi_{c,\mathrm{int}} = 0$ |
| $A_{\mathrm{sum}} \neq 0$; $\pi + \phi_{\mathrm{sum}} \in$ (13); | $\varphi_{a,\mathrm{int}} = \varphi_{a,1} + \varphi_{a,\mathrm{pre}} - (\pi + \phi_{\mathrm{sum}})$, $\varphi_{b,\mathrm{int}} = \varphi_{c,\mathrm{int}} = 0$ |
| $A_{\mathrm{sum}} \neq 0$; $\pi + \phi_{\mathrm{sum}} \notin$ (13); $g(\phi_{a,\min}) < g(\phi_{a,\max})$; | $\varphi_{a,\mathrm{int}} = 2\pi(1\text{-}D_{p,a})$, $\varphi_{b,\mathrm{int}} = \varphi_{c,\mathrm{int}} = 0$ |
| $A_{\mathrm{sum}} \neq 0$; $\pi + \phi_{\mathrm{sum}} \notin$ (13); $g(\phi_{a,\min}) \geq g(\phi_{a,\max})$; | $\varphi_{a,\mathrm{int}} = \varphi_{b,\mathrm{int}} = \varphi_{c,\mathrm{int}} = 0$ |

3) *One 1P Converter Operates in TCCM*: In this scenario, only one converter is unable to undergo phase adjustment, leading to one of the three independent variables of the function $g(\phi_a, \phi_b, \phi_c)$ being constant. The C-phase converter operating in TCCM is analyzed as an illustrative example. The same conclusions will be obtained by analyzing using two other 1P converters; therefore, they will not be repeated here. In this context, $g(\phi_a, \phi_b)$ can be reduced to a binary function of $\phi_a$ and $\phi_b$. The feasible regions of the independent variables of the function $g(\phi_a, \phi_b)$ are shown in (17), and the function's partial derivatives are represented by (18). The condition for $g(\phi_a, \phi_b)$ to obtain extreme values can be obtained by setting $g_1'(\phi_a, \phi_b)$ and $g_2'(\phi_a, \phi_b)$ equal to zero

$$\begin{cases} \phi_a \in [\phi_{a,\min}, \phi_{a,\max}] \\ \phi_{a,\max} = \mathrm{farg}(\varphi_{a,1} + \varphi_{a,\mathrm{pre}}) \\ \phi_{a,\min} = \mathrm{farg}(\varphi_{a,1} + \varphi_{a,\mathrm{pre}} - 2\pi(1 - D_{p,a})) \end{cases} \tag{17a}$$

TABLE III
OPSA WHEN ONE 1P CONVERTER OPERATE IN TCCM

| Condition | OPSA of three 1P converters |
|---|---|
| $A_{a,1}=0, A_{b,1}\neq 0$; farg$(\pi+\phi_c)\in$ (17b) | $\varphi_{a,\text{int}}=\varphi_{c,\text{int}}=0$, $\varphi_{b,\text{int}}=\varphi_{b,1}+\varphi_{b,\text{pre}}-(\pi+\phi_c)$ |
| $A_{a,1}=0, A_{b,1}\neq 0$; farg$(\pi+\phi_c)\notin$ (17b); $g(\phi_{a,\min})<g(\phi_{a,\max})$ | $\varphi_{a,\text{int}}=\varphi_{c,\text{int}}=0$, $\varphi_{b,\text{int}}=2\pi(1\text{-}D_{p,b})$ |
| $A_{a,1}=0, A_{b,1}\neq 0$; farg$(\pi+\phi_c)\notin$ (17b); $g(\phi_{a,\min})\geq g(\phi_{a,\max})$ | $\varphi_{a,\text{int}}=\varphi_{b,\text{int}}=\varphi_{c,\text{int}}=0$ |
| $A_{b,1}=0, A_{a,1}\neq 0$; farg$(\pi+\phi_c)\in$ (17a); | $\varphi_{b,\text{int}}=\varphi_{c,\text{int}}=0$, $\varphi_{a,\text{int}}=\varphi_{a,1}+\varphi_{a,\text{pre}}-(\pi+\phi_c)$ |
| $A_{b,1}=0, A_{a,1}\neq 0$; farg$(\pi+\phi_c)\notin$ (17a); $g(\phi_{a,\min})<g(\phi_{a,\max})$ | $\varphi_{b,\text{int}}=\varphi_{c,\text{int}}=0$, $\varphi_{a,\text{int}}=2\pi(1\text{-}D_{p,a})$ |
| $A_{b,1}=0, A_{a,1}\neq 0$; farg$(\pi+\phi_c)\notin$ (17a); $g(\phi_{a,\min})\geq g(\phi_{a,\max})$; | $\varphi_{a,\text{int}}=\varphi_{b,\text{int}}=\varphi_{c,\text{int}}=0$ |
| $A_{b,1}\neq 0, A_{a,1}\neq 0$; $\forall\, x,y,z\in\{A_{a,1},A_{b,1},A_{c,1}\}, x+y>z$; (20) $\in$ (17); | $\varphi_{c,\text{int}}=0$, using (20) to obtain $\phi_a$, $\phi_b$; $\varphi_{x,\text{int}}=\phi_{x,\max}-\phi_x$, $x=a,b$ |
| $A_{b,1}\neq 0, A_{a,1}\neq 0$; $\exists\, x,y,z\in\{A_{a,1},A_{b,1},A_{c,1}\}, x+y\leqslant z$; (20) $\in$ (17); | $\varphi_{c,\text{int}}=0$, using (22) to obtain $\phi_a$, $\phi_b$; $\varphi_{x,\text{int}}=\phi_{x,\max}-\phi_x$, $x=a,b$ |
| $A_{b,1}\neq 0, A_{a,1}\neq 0$; (20) $\notin$ (17b); $\exists\, x\in\{\phi_{a,\min},\phi_{a,\max}\}, \exists\, y\in\{\phi_{b,\min},\phi_{b,\max}\}$, $g(x,y)=$ (23); | $\varphi_{a,\text{int}}=\phi_{a,\max}-x$, $\varphi_{b,\text{int}}=\phi_{b,\max}-y$, $\varphi_{c,\text{int}}=0$ |

$$\begin{cases}\phi_b\in[\phi_{b,\min},\phi_{b,\max}]\\ \phi_{b,\max}=\text{farg}(\varphi_{b,1}+\varphi_{b,\text{pre}})\\ \phi_{b,\min}=\text{farg}(\varphi_{b,1}+\varphi_{b,\text{pre}}-2\pi(1-D_{p,b}))\end{cases}\tag{17b}$$

$$g_1'(\phi_a,\phi_b)=2A_{a,1}\left[A_{b,1}\sin(\phi_b-\phi_a)-A_{c,1}\sin(\phi_a-\phi_c)\right]\tag{18a}$$

$$g_2'(\phi_a,\phi_b)=2A_{b,1}\left[A_{a,1}\sin(\phi_a-\phi_b)-A_{c,1}\sin(\phi_b-\phi_c)\right].\tag{18b}$$

In the event that either $A_{a,1}$ or $A_{b,1}$ is equal to zero, for instance, when $A_{b,1}$ is set to zero, the value of $\phi_b$ ceases to impact the function $g(\phi_a, \phi_b)$. Thus, $\phi_b$ can take any value within its feasible region. To streamline the phase shift operation, the value of $\varphi_{b,\text{int}}$ is set to zero. This situation is analogous to Scenario 2, where the function $g(\phi_a, \phi_b, \phi_c)$ is a unary function about $\phi_a$. Therefore, the previously established conclusion can be applied, thereby indicating that the function attains minimal value at $\phi_a=\pi+\phi_c$. Subsequently, it is imperative to ascertain whether the value falls within the adjustable range. The judgment method is analogous to Scenario 2 and will not be reiterated. The results of the analysis are enumerated in Table III. It is noteworthy that the situation $A_{a,1}=0$ is analogous to that $A_{b,1}=0$, and the results are also presented directly in Table III.

In the event that both $A_{a,1}$ and $A_{b,1}$ are not equal to zero, the solution to the system of equations $g_1'(\phi_a, \phi_b)=0$ and $g_2'(\phi_a, \phi_b)=0$ results in the (19). It is evident that (19a) is the formula description of the law of sines. This is to say, the minimum

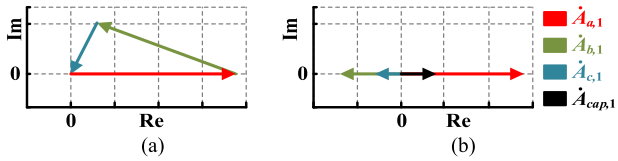


Fig. 7. (a) Case in which three phasors are able to form a closed triangle. (b) Case in which three vectors are unable to form a closed triangle.

value is attained when the three phasors form a closed triangle, as shown in Fig. 7(a). Pursuant to the properties of triangles, this case necessitates that the moduli of the three phasors satisfy the following relationship: "the sum of two sides is greater than the third side." The argument angle of each phasor can then be obtained by the law of cosines, as shown in (20)

$$\frac{A_{b,1}}{\sin(\phi_a-\phi_c)}=\frac{A_{c,1}}{\sin(\phi_b-\phi_a)}=\frac{A_{a,1}}{\sin(\phi_c-\phi_b)}\tag{19a}$$

$$\sin(\phi_b-\phi_a)=\sin(\phi_a-\phi_c)=\sin(\phi_c-\phi_b)=0\tag{19b}$$

$$\begin{cases}\phi_a=\text{farg}\left(\phi_c+\pi-\arccos\left(\frac{A_{a,1}^2+A_{c,1}^2-A_{b,1}^2}{2A_{a,1}A_{c,1}}\right)\right)\\ \phi_b=\text{farg}\left(\phi_c-\pi+\arccos\left(\frac{A_{b,1}^2+A_{c,1}^2-A_{a,1}^2}{2A_{b,1}A_{c,1}}\right)\right)\end{cases}.\tag{20}$$

Conversely, when the moduli of the three phasors fail to meet the properties of triangles, (19b) can be solved to determine that the function $g(\phi_a, \phi_b)$ attains an extreme value when the argument angles of the three phasors satisfy (21). Then, in conjunction with the nature of the phasor, the nonzero minimum phasor sum is obtained when the phasor with the greatest modulus is oriented at an argument angle of "$\pi$" in relation to the other two phasors. For example, considering the operational condition depicted in Fig. 7(b), where $A_{a,1}>A_{b,1}>A_{c,1}$, the argument angle of each phasor that yield a minimum phasor sum are delineated in (21)

$$\phi_a,\phi_b\in\{\text{farg}(\pi+\phi_c),\phi_c\}\tag{21}$$

$$\phi_a=\phi_b=\text{farg}(\pi+\phi_c).\tag{22}$$

Equations (20) and (22) represent the values of the independent variables when the functiong$(\phi_a, \phi_b)$ attains its minimum value, according to the properties of the function. However, the constraints on the range of values of the independent variables are not taken into account in the aforementioned solution process. Consequently, it is essential to verify whether the value lies within the feasible region, that is, to determine whether the values of (20) and (22) are within the interval of (17). If it does, one can proceed to utilize (20) and (22) to determine the associated PSAs, as presented in Table III. Conversely, if the value does not fall within this region, it becomes imperative to further analyze the function to ascertain its minimum value within the bounded closed interval.

$$g'_1(\phi_a)=2A_{a,1}A_{\text{sum}}\sin(\phi_{\text{sum}}-\phi_a),\begin{cases}\phi_{\text{sum}}=\text{atan2}\left[\sum_{x=b,c}A_{x,1}\sin(\phi_x),\sum_{x=b,c}A_{x,1}\cos(\phi_x)\right]\\ A_{\text{sum}}=\sqrt{\left[\sum_{x=b,c}A_{x,1}\sin(\phi_x)\right]^2+\left[\sum_{x=b,c}A_{x,1}\cos(\phi_x)\right]^2}\end{cases}\tag{15}$$

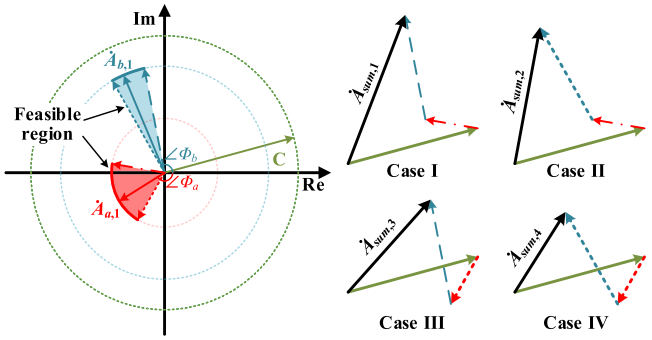


Fig. 8. Scenario where C-phase is operating in TCCM while A-phase and B-phase are operating in TDCM.

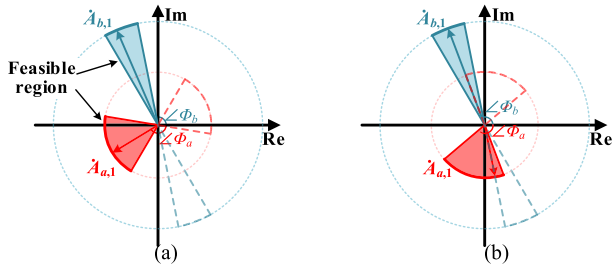


Fig. 9. Scenario where three 1P converters operating in TDCM, $A_{c,1} = 0$. (a) OPSAs fall outside the feasible region. (b) OPSAs fall inside the feasible region.

As the function $g(\phi_a, \phi_b)$ has no additional extreme points, if the OPSAs derived from (20) and (22) exceed the feasible region, the OPSA sought must be obtained at the boundary of the feasible region. As illustrated in Fig. 8, there are four potential combinations. To identify the OPSA, it is sufficient to substitute each of the four sets of boundary values into $g(\phi_a, \phi_b)$. The determination of the OPSA is achieved by substituting each of the four sets of boundary values into the function $g(\phi_a, \phi_b)$, thus yielding the minimum of these four sets of results, as illustrated in (23). The OPSA is then obtained by identifying the set of boundary values that minimizes the value taken by the function $g(\phi_a, \phi_b)$. The results are given in Table III

$$g_{\min}(\phi_a, \phi_b) = \min \begin{bmatrix} g(\phi_{a,\min}, \phi_{b,\min}), g(\phi_{a,\min}, \phi_{b,\max}), \\ g(\phi_{a,\max}, \phi_{b,\min}), g(\phi_{a,\max}, \phi_{b,\max}) \end{bmatrix}. \tag{23}$$

4) *Three 1P Converters Operate in TDCM*: In this scenario, all three 1P converters are able to undergo phase adjustment. The feasible regions of the independent variables of the function $g(\phi_a, \phi_b, \phi_c)$ are shown in (24), and the partial derivatives of $g(\phi_a, \phi_b, \phi_c)$ with respect to the three variables in this scenario can be expressed as in (25). By setting the partial derivatives to zero, it can be obtained that the conditions for the function $g(\phi_a, \phi_b, \phi_c)$ to attain an extremum in this scenario are identical to those in Scenario 3, as given in (19)

$$\begin{cases} \phi_a \in [\phi_{a,\min}, \phi_{a,\max}] \\ \phi_{a,\max} = \operatorname{farg}(\varphi_{a,1} + \varphi_{a,\text{pre}}) \\ \phi_{a,\min} = \operatorname{farg}(\varphi_{a,1} + \varphi_{a,\text{pre}} - 2\pi(1 - D_{p,a})) \end{cases} \tag{24a}$$

$$\begin{cases} \phi_b \in [\phi_{b,\min}, \phi_{b,\max}] \\ \phi_{b,\max} = \operatorname{farg}(\varphi_{b,1} + \varphi_{b,\text{pre}}) \\ \phi_{b,\min} = \operatorname{farg}(\varphi_{b,1} + \varphi_{b,\text{pre}} - 2\pi(1 - D_{p,b})) \end{cases} \tag{24b}$$

$$\begin{cases} \phi_c \in [\phi_{c,\min}, \phi_{c,\max}] \\ \phi_{c,\max} = \operatorname{farg}(\varphi_{c,1} + \varphi_{c,\text{pre}}) \\ \phi_{c,\min} = \operatorname{farg}(\varphi_{c,1} + \varphi_{c,\text{pre}} - 2\pi(1 - D_{p,c})) \end{cases} \tag{24c}$$

$$g_1'(\phi_a, \phi_b, \phi_c) = 2A_{a,1} [A_{b,1}\sin(\phi_b - \phi_a) - A_{c,1}\sin(\phi_a - \phi_c)] \tag{25a}$$

$$g_2'(\phi_a, \phi_b, \phi_c) = 2A_{b,1} [A_{a,1}\sin(\phi_a - \phi_b) - A_{c,1}\sin(\phi_b - \phi_c)] \tag{25b}$$

$$g_3'(\phi_a, \phi_b, \phi_c) = 2A_{c,1} [A_{a,1}\sin(\phi_a - \phi_c) - A_{b,1}\sin(\phi_c - \phi_b)]. \tag{25c}$$

In the event that any of $A_{a,1}, A_{b,1}$, or $A_{c,1}$ is equal to zero, the conditions for the function $g(\phi_a, \phi_b, \phi_c)$ to take extreme values can only be derived from (19b). For instance, when $A_{c,1}$ is set to zero, the value of $\phi_c$ ceases to impact the function $g(\phi_a, \phi_b, \phi_c)$. Thus, $\phi_c$ can take any value within its feasible region. To streamline the phase shift operation, the value of $\varphi_{c,\text{int}}$ is set to zero. According to the previous conclusions, the condition for the function $g(\phi_a, \phi_b, \phi_c)$ to attain a minimum value in this instance is that the argument angles of $\dot{A}_{a,1}$ and $\dot{A}_{b,1}$ differ by 180°, as shown in (26). In order to calculate the OPSAs, the two possible cases in Fig. 9 are analyzed. The feasible region of $\phi_a$ and $\phi_b$ is illustrated with red shading and blue shading, respectively. Subsequently, two regions, demarcated by red dashed and blue dotted lines, respectively, are obtained after rotating these two feasible regions by 180°. It is evident from Fig. 9(a) that the red shaded region does not coincide with the blue dashed region, indicating that no value within the feasible region can satisfy condition (26). In order to minimize the function within the bounded closed interval, it is necessary to make the difference between $\phi_a$ and $\phi_b$ as close to $\pi$ as possible. Therefore, the value of the variables that minimizes the function $g(\phi_a, \phi_b, \phi_c)$ must be at the boundary of the feasible region. In Fig. 9(b), there exists an infinite number of combinations that satisfy (26) within the area where the dashed and shaded regions overlap. This indicates that the PSA combinations that minimize the function are numerous, but regardless of how the overlapping region changes, the boundary values of the feasible region are always included.

According to the foregoing analysis, it can be determined that in order to minimize the function $g(\phi_a, \phi_b, \phi_c)$, at least one of $\phi_a$ and $\phi_b$ must be equal to the boundary value of the feasible region. Then, the determination of the OPSA that allows the function to achieve a minimum value is presented in the first two rows of Table IV

$$|\phi_a - \phi_b| = \pi \tag{26}$$

TABLE IV
OPSA WHEN THREE 1P CONVERTERS OPERATE IN TCCM

| Condition | OPSA of three 1P converters |
|---|---|
| $A_{c,1}=0, A_{b,1}\neq 0, A_{a,1}\neq 0$; $\exists\, x\in\{\text{farg}(\pi+\phi_{b,\max}), \text{farg}(\pi+\phi_{b,\min})\}, x\in$ (24a); | $\varphi_{c,\text{int}}=0$, $\varphi_{a,\text{int}}=\varphi_{a,1}+\varphi_{a,\text{int}}-x$, $\varphi_{b,\text{int}}=\varphi_{b,1}+\varphi_{b,\text{int}}-\text{farg}(\pi+x)$, |
| $A_{c,1}=0, A_{b,1}\neq 0, A_{a,1}\neq 0$; $\forall\, x\in\{\text{farg}(\pi+\phi_{b,\max}), \text{farg}(\pi+\phi_{b,\min})\}, x\notin$ (24a); $\forall\, y\in\{\phi_{a,\min},\phi_{a,\max}\}, \forall\, z\in\{\phi_{b,\min},\phi_{b,\max}\}, g(y,z)=$ (27); | $\varphi_{a,\text{int}}=\phi_{a,\max}-y$, $\varphi_{b,\text{int}}=\phi_{b,\max}-z$, $\varphi_{c,\text{int}}=0$ |
| $A_{a,1}\neq 0, A_{b,1}\neq 0, A_{c,1}\neq 0$; $\forall\, x, y, z\in\{A_{a,1}, A_{b,1}, A_{c,1}\}, x+y>z$; $\exists\, l\in$ (30), (28) $\in$ (24); | $\phi_{\text{cm}}=l$, using (28) to obtain $\phi_a$, $\phi_b$, $\phi_c$; $\varphi_{x,\text{int}}=\phi_{x,\max}-\phi_x$, $x=a,b,c$ |
| $A_{a,1}\neq 0, A_{b,1}\neq 0, A_{c,1}\neq 0$; $\exists\, x, y, z\in\{A_{a,1}, A_{b,1}, A_{c,1}\}, x+y\leqslant z$; $\exists\, l\in$ (30), (29) $\in$ (24); | $\phi_{\text{cm}}=l$, using (29) to obtain $\phi_a$, $\phi_b$, $\phi_c$; $\varphi_{x,\text{int}}=\phi_{x,\max}-\phi_x$, $x=a,b,c$ |
| $A_{a,1}\neq 0, A_{b,1}\neq 0, A_{c,1}\neq 0$; $\forall\, l\in$ (30), (28) $\notin$ (24); $\forall\, l\in$ (30), (29) $\notin$ (24); $\exists\, x\in\{\phi_{a,\min},\phi_{a,\max}\}, \exists\, y\in\{\phi_{b,\min},\phi_{b,\max}\}$, $\exists\, z\in\{\phi_{c,\min},\phi_{c,\max}\}, g(x,y,z)=$ (31); | $\varphi_{a,\text{int}}=\phi_{a,\max}-x$, $\varphi_{b,\text{int}}=\phi_{b,\max}-y$, $\varphi_{c,\text{int}}=\phi_{c,\max}-z$ |

$$\begin{cases}\Delta\phi_{ab,\max}=\max\left[|\text{farg}\left(\phi_a-\phi_b\right)|\right]\\ \phi_a=\{\phi_{a,\min},\phi_{a,\max}\}, \phi_b=\{\phi_{b,\min},\phi_{b,\max}\}\end{cases}. \tag{27}$$

In the event that none of $A_{a,1}, A_{b,1}$, or $A_{c,1}$ is equal to zero, it is necessary to select different formulas to calculate the OPSA according to the magnitude relationship between $A_{a,1}, A_{b,1}$, and $A_{c,1}$. In instances where the sum of any two of $A_{a,1}, A_{b,1}$, or $A_{c,1}$ exceeds the third, the solution to (19a) can be utilized to ascertain the value of the independent variable for which the function $g(\phi_a, \phi_b, \phi_c)$ attains its minimum value, as shown in (28). Conversely, in instances where the relationship between $A_{a,1}$, $A_{b,1}$, and $A_{c,1}$ does not satisfy the aforementioned conditions, for instance, when $A_{a,1} > A_{b,1} + A_{c,1}$, it is possible to solve (19b) to obtain a solution that allows the function $g(\phi_a, \phi_b, \phi_c)$ to attain a minimum value, as shown in (29), where $\phi$cm is a constant term that can be set to any value between $-\pi$ and $\pi$. By adjusting the value of $\phi$cm, the values of (28) and (29) can be altered so that they fall in the feasible region as much as possible

$$\begin{cases}\phi_a=\phi_{\text{cm}}\\ \phi_b=\text{farg}\left(\phi_{\text{cm}}+\pi-\arccos\left(\frac{A_{a,1}^2+A_{b,1}^2-A_{c,1}^2}{2A_{a,1}A_{b,1}}\right)\right)\\ \phi_c=\text{farg}\left(\phi_{\text{cm}}+\pi+\arccos\left(\frac{A_{a,1}^2+A_{c,1}^2-A_{b,1}^2}{2A_{a,1}A_{c,1}}\right)\right)\end{cases} \tag{28}$$

$$\phi_a=\varphi_{\text{cm}}; \phi_b=\pi+\varphi_{\text{cm}}; \phi_c=\pi+\varphi_{\text{cm}}. \tag{29}$$

Fig. 10 illustrates the set of phasors obtained under identical operating conditions, given disparate $\phi$cm. The OPSA in Fig. 10(a) and (b) are both fall within the feasible region. The key distinction between Fig. 10(a) and (b) is that the value of $\phi_a$ in Fig. 10(b) is taken at the boundary of the feasible region. A comparison of the two figures reveals that the previously established conclusion regarding the OPSA, which states that "a value of OPSA will invariably be found at the boundary of the feasible region," remains valid in this case. Six values of $\phi$cm can be obtained based on the six boundaries of the feasible region, as given in (30). Subsequently, by substituting the values

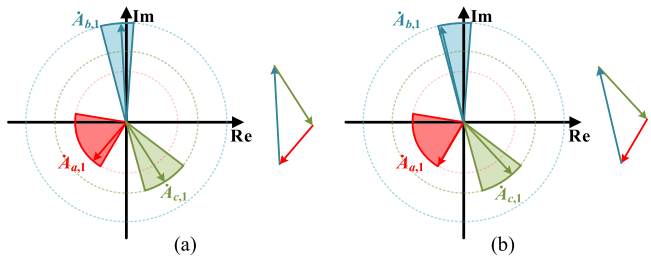


Fig. 10. Scenario where three 1P converters operating in TDCM. (a) OPSAs fall inside the feasible region, $\phi$cm = -130°. (b) OPSAs fall inside the feasible region, $\phi$ cm $=-120°$.

of $\phi$cm into (28) or (29), respectively, and determining whether the obtained values are within the interval of (24), it can be ascertained whether the corresponding solution is within the feasible region.

$$\varphi_{\text{cm}}\in\begin{Bmatrix}\phi_{a,\min},\phi_{a,\max},\phi_{b,\min}+\arccos\left(\frac{A_{a,1}^2+A_{b,1}^2-A_{c,1}^2}{2A_{a,1}A_{b,1}}\right)-\pi,\\ \phi_{b,\max}+\arccos\left(\frac{A_{a,1}^2+A_{b,1}^2-A_{c,1}^2}{2A_{a,1}A_{b,1}}\right)-\pi,\\ \phi_{c,\min}-\pi-\arccos\left(\frac{A_{a,1}^2+A_{c,1}^2-A_{b,1}^2}{2A_{a,1}A_{c,1}}\right),\\ \phi_{c,\max}-\pi-\arccos\left(\frac{A_{a,1}^2+A_{c,1}^2-A_{b,1}^2}{2A_{a,1}A_{c,1}}\right)\end{Bmatrix} \tag{30}$$

$$\begin{cases}g_{\min}(\phi_a,\phi_b,\phi_c)=\min\left[g(x,y,z)\right]\\ x\in[\phi_{a,\min},\phi_{a,\max}], y\in[\phi_{b,\min},\phi_{b,\max}], z\\ \qquad\in[\phi_{c,\min},\phi_{c,\max}]\end{cases} \tag{31}$$

In the event that none of the aforementioned six sets of OPSA are within the feasible region, the function $g(\phi_a, \phi_b, \phi_c)$ attains a minimum value when $\phi_a, \phi_b$, and $\phi_c$ are all equal to the boundary values, the eight sets of values are given in (31).

To summarize the analysis presented above, the all solution of OPSA when all three 1P converters are operating in TDCM are enumerated in Table IV.

### C. Practical Implementation and Algorithm Design

Based on the results presented in Section III-B, a control algorithm can be established. A flowchart of the algorithm is shown in Fig. 11(a). Three steps are required to implement harmonic current elimination in the controller. The first step is to obtain the information of LFHC using (5). For the harmonics selected for elimination ($k = 1$), their Fourier coefficients are related only to the voltage transfer ratio and the variables $D_p$, $D_s$, and $D_f$, which are determined by the operating point and are accessible in the closed-loop control program. The second step is to solve for the argument angles that minimizes (10). This is obtained by substituting the harmonic information obtained in the first step into (28) and (29). The third step involves verifying whether the solution obtained in the second step falls within the feasible region. The various solution sets corresponding to the four different scenarios have been enumerated in Tables II–IV, and they can be found according to the conditions.

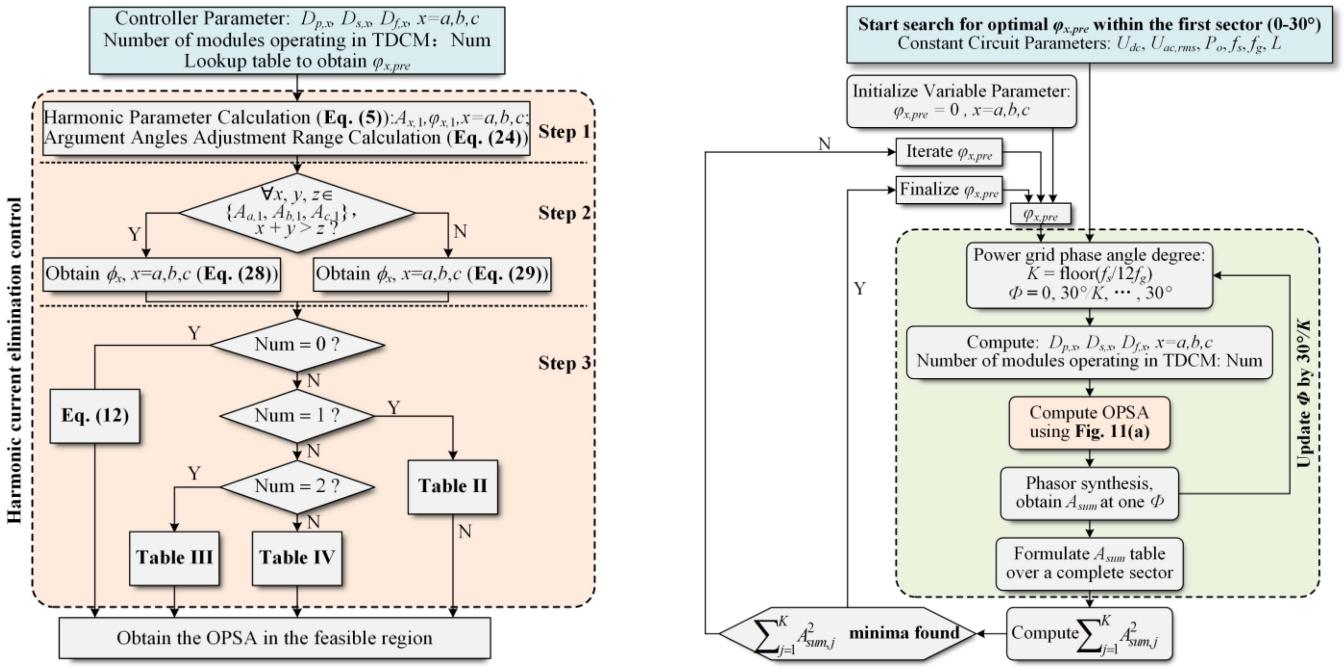


(a) (b)

Fig. 11. (a) Flowchart of the calculation of $\varphi_{x,\text{int}}$. (b) Flowchart of the calculation of $\varphi_{x,\text{pre}}$.

TABLE V
MAPPING OF PARAMETERS IN DIFFERENT SECTORS

| | 0°–30°, 180°–210° | 30°–60°, 210°–240° | 60°–90°, 240°–270° | 90°–120°, 270°–300° | 120°–150°, 300°–330° | 150°–180°, 330°–360° |
|---|---|---|---|---|---|---|
| $\varphi_{a,\text{pre}}$ | Ref_$\varphi_a$ | Ref_$\varphi_c$ | Ref_$\varphi_b$ | Ref_$\varphi_b$ | Ref_$\varphi_c$ | Ref_$\varphi_a$ |
| $\varphi_{b,\text{pre}}$ | Ref_$\varphi_b$ | Ref_$\varphi_b$ | Ref_$\varphi_c$ | Ref_$\varphi_a$ | Ref_$\varphi_a$ | Ref_$\varphi_c$ |
| $\varphi_{c,\text{pre}}$ | Ref_$\varphi_c$ | Ref_$\varphi_a$ | Ref_$\varphi_a$ | Ref_$\varphi_c$ | Ref_$\varphi_b$ | Ref_$\varphi_b$ |

The aforementioned computations regarding $\varphi_{x,\text{int}}$ are performed in real-time by the controller once the converter has reached a steady state. Moreover, $\varphi_{x,\text{pre}}$ requires offline optimization to develop a second order lookup table (LUT) based on output power and dc voltage. This segment of the optimization process is executed using Mathcad, and the algorithm's implementation flowchart is illustrated in Fig. 11(b). The judgment condition for the optimum $\varphi_{x,\text{pre}}$ is such that the rms value of LFHC is minimized in the 0°–30° sector. The LUT is constructed in 20 V voltage steps and 10% load factor steps to obtain a total of 100 sets of data, each containing three values that were stored in the controller. The correspondence between these three values in different sectors is demonstrated in Table V, where Ref_$\varphi_a$ ($x=a, b, c$) represents the data read from the LUT. The manner in which the sectors are divided is shown in Fig. 1(b).

## IV. EXPERIMENTAL TEST

An experimental platform contains three identical DAB 1P1Sac-dc converters was built to verify the effectiveness of the proposed method. Fig. 12 shows annotated photographs of the hardware and Table VI lists the converter specifications and parameters of passive components. The semiconductor devices used in the SR bridge are SJ MOSFET (ASW50R130E from ANHI). The semiconductor devices used in the DAB are SiC MOSFET (IMZA65R057M1HXKSA1 for the ac-side active bridge and CCB032M12FM3 for the dc-side active bridge, both are from Infineon and CREE, respectively. Three-phase SiC modules are used to better monitor the dc side rectified current).

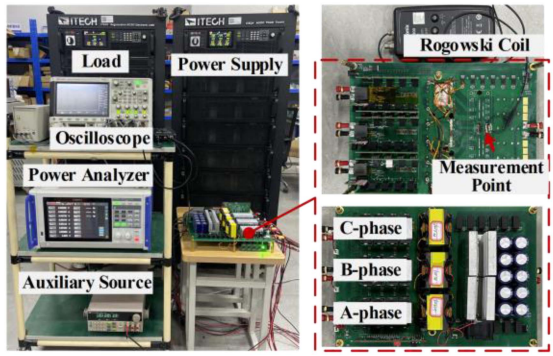


Fig. 12. Experimental platform.

TABLE VI
NOMINAL OPERATING CONDITIONS AND CONVERTER SPECIFICATIONS

| Symbol | Description | Value |
|---|---|---|
| $u_{ac}$ | Input voltage (line-to-neutral) | 110 Vrms, 50 Hz |
| $u_{\text{dc}}$ | DC output voltage | 200–400 V |
| $L$ | Phase shift inductor | 40 $\mu$H |
| $f_s$ | Switching frequency | 25 kHz |
| $n:1$ | Transformer turns ratio | 0.5 : 1 |
| $C_{\text{bus}}$ | DC bus capacitor | 1 mF |
| $L_f$ | AC side filter inductor | 188 $\mu$H |
| $C_f$ | AC side filter capacitor | 8.8 $\mu$F |
| $P$ | Rated output power | 3×1.1 kW |

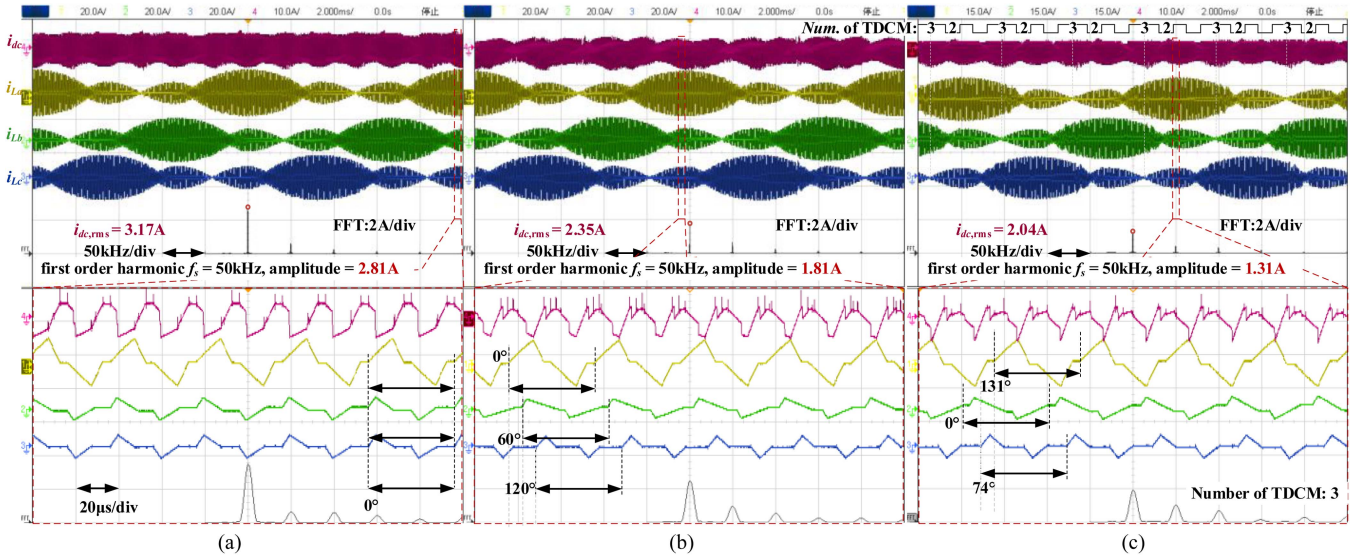


Fig. 13. Steady-state experimental current waveforms and DC-link capacitor ripple current spectrum, $u_{\rm dc} = 200$ V, $P_o = 900$ W. ($i_{\rm dc}$—DC side total ripple current, $i_{La}$, $i_{Lb}$, and $i_{Lc}$—the DAB stage inductor currents). (a) ZPST (0° phase shift). (b) UPST (120° phase shift). (c) Proposed.

TABLE VII
SELECTED COMPONENTS

| | |
|---|---|
| Transformer Core | PQ5050, PC95, 1 pair |
| Primary Winding | 0.1 mm litz wire, 150 strands, 32 turns |
| Secondary Winding | 0.1 mm litz wire, 150 strands, 64 turns |
| Measured Inductance | Leakage inductance 18.1 $\mu$H, w.r.t. to primary<br>Magnetic inductance 30.4 mH, w.r.t. to primary |
| Series Inductor Core | NPC107060, 2 pairs stacked |
| Winding | 0.1 mm litz wire, 150 strands, 12 turns |
| Measured Inductance | 22 $\mu$H |
| $C_{\rm bus}$ | 10 × LKZK4002J101MF, 100 $\mu$F, 600 V |
| $L_f$ | CODACA 4 × CSM2214-470M, 47 $\mu$H |
| $C_f$ | TDK 4 × C5750X6S2W225KT000N, 2.2 $\mu$F, 450 V |

The model numbers and design parameters of the remaining passive components are presented in Table VII. To implement the proposed method, all three converters are controlled by an identical control board. This allows for precise timing of the three converters without the requirement to synchronize controllers. The Rogowski coil (Tektronix TRCP0300) is used to measure the rectified current $i_{dc}$ on the dc side. The bandwidth of this current sensor is 9 Hz–30 MHz, thereby enabling precise measurement of the ripple current. Due to the removal of the dc component, the ripple current $i_{\rm dc}$ can be regarded as that which flows into the capacitor.

Experiments were conducted on the DAB-3P1S ac–dc converter in rectifier mode to further demonstrate the validity of the proposed method. The experiment encompasses three distinct scenarios ($G_m$ is the ratio of the peak grid voltage to $nu_{\rm dc}$).

1) *Case I:* Fig. 13 illustrates the waveform and frequency spectrum of TCRC, which were derived utilizing three distinct phase shift techniques. The zero-phase-shift technique (ZPST) is achieved by configuring the PSA among three 1P converters to 0°, while the UPST is accomplished by setting the PSA among three 1P converters to 120°. These measurements were conducted at a load rate of 50%, with the output voltage maintained at 200 V, corresponding to a $G_m$ greater than one. FFT is used to verify the elimination effect of the LFHC. To facilitate the comparison, the experimental data were organized and subsequently converted into a bar chart in Fig. 17. The utilization of UPST led to a reduction in the rms values of LFHC and TCRC by 35.6% and 25.9%, respectively. The method proposed in this article yielded a 53.4% and 35.6% reduction in rms values for LFHC and TCRC, respectively. The experimental result shows that, in contrast to the UPST, the proposed method in this study markedly decreases the LFHC and evidently diminishes the rms value of the TCRC. Furthermore, (32) is employed to evaluate the LFHC share in TCRC. $i_{\rm LFHC,rms}$ and $i_{\rm TCRC,rms}$ denote the rms values of LFHC and TCRC, respectively. The values of λ obtained using UPST and the proposed method are 29.7% and 20.6%, respectively, which indicates that the LFHC share in the TCRC basically obtained by the proposed method decreases obviously

$$\lambda = i^2_{\rm LFHC,rms} / i^2_{\rm TCRC,rms}. \tag{32}$$

2) *Case II:* Fig. 14 illustrates the waveform and frequency spectrum of TCRC, which were derived utilizing three distinct phase shift techniques. These measurements were conducted at a load rate of 100%, with the output voltage maintained at 300 V, corresponding to a $G_m$ approximately equal to one. The experimental data were organized and presented in Fig. 17. The utilization of UPST led to a reduction in the rms values of LFHC and TCRC by 60% and 44.4%, respectively. The proposed method yielded a 93.3% and 59.4% reduction in rms values for LFHC and TCRC, respectively. The values of λ obtained using UPST and the proposed method are 8.7% and 1.1%, respectively. The experimental results demonstrate that the method proposed in this article exhibits superior ripple elimination efficacy. Furthermore, owing to the mirror

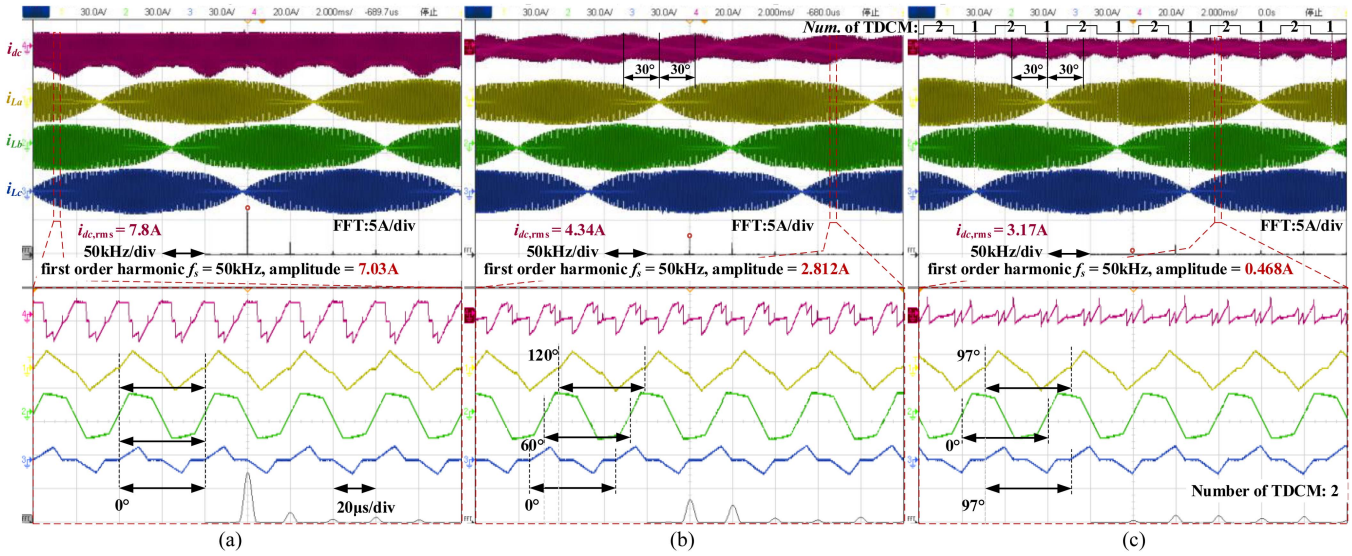


Fig. 14. Steady-state experimental current waveforms and DC-link capacitor ripple current spectrum, $u_{\rm dc} = 300$ V, $P_o = 2700$ W. ($i_{\rm dc}$—DC side total ripple current, $i_{La}$, $i_{Lb}$, and $i_{Lc}$—the DAB stage inductor currents). (a) ZPST (0° phase shift). (b) UPST (120° phase shift). (c) Proposed.

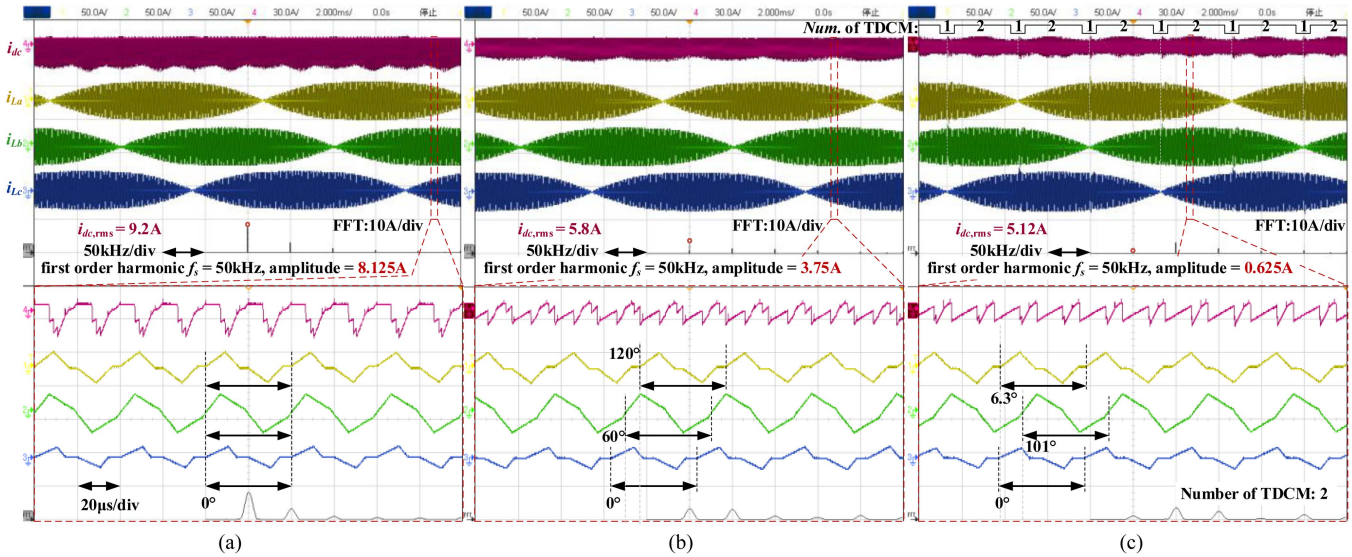


Fig. 15. Steady-state experimental current waveforms and DC-link capacitor ripple current spectrum, $u_{\rm dc} = 400$ V, $P_o = 3300$ W. ($i_{\rm dc}$—DC side total ripple current, $i_{La}$, $i_{Lb}$, and $i_{Lc}$—the DAB stage inductor currents). (a) ZPST (0° phase shift). (b) UPST (120° phase shift). (c) Proposed.

image relationship that exists between adjacent sectors, optimal ripple cancellation can only be achieved by employing different combinations of $\varphi_{x,\rm pre}$ across different sectors. This phenomenon is particularly illustrated in Fig. 14(b) and (c), which demonstrate that the envelope curve of TCRC generated by the UPST demonstrate distinct variations across adjacent sectors. Conversely, the envelope curve of TCRC produced by the proposed method also exhibit a mirror-image characteristic. This is reason why the proposed method has better ripple elimination effect.

3) *Case III:* Fig. 15 illustrates the waveform and frequency spectrum of TCRC, which were derived utilizing three distinct phase shift techniques. These measurements were conducted at a load rate of 100%, with the output voltage maintained at 400 V, corresponding to a $G_m$ less than one. The experimental data were organized and presented in Fig. 17. The utilization of UPST led to a reduction in the rms values of LFHC and TCRC by 53.9% and 37%, respectively. The proposed method yielded a 92.3% and 44.3% reduction in rms values for LFHC and TCRC, respectively. The values of λ obtained using UPST and the proposed method are 20.9% and 0.75%, respectively. The experimental results demonstrate that the proposed method exhibits superior ripple elimination efficacy. Furthermore, the waveforms generated by three distinct phase-shift techniques are analyzed at the 145° phase angle of grid phase A, revealing detailed switching-cycle current characteristics. As illustrated in the Figs. 13–15, each technique employs different phase configurations,

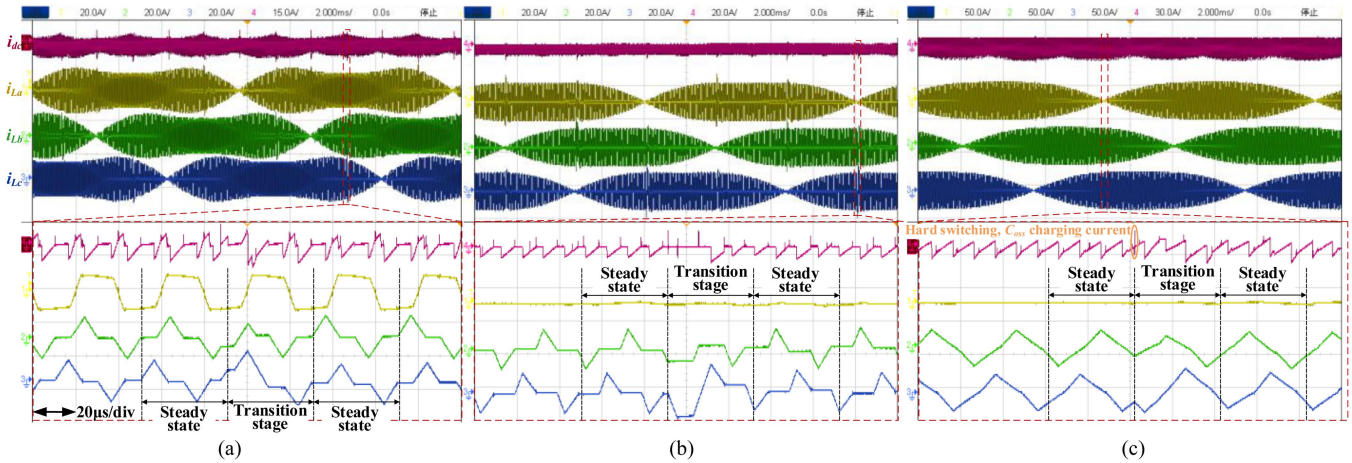


Fig. 16. Steady-state experimental current waveforms and DC-link capacitor ripple current spectrum with the proposed method. ($i_{\rm dc}$—DC side total ripple current, $i_{La}$, $i_{Lb}$, and $i_{Lc}$—the DAB stage inductor currents). (a) 300 V, 1800 W. (b) 400 V, 825 W. (c) 400 V, 3300 W.

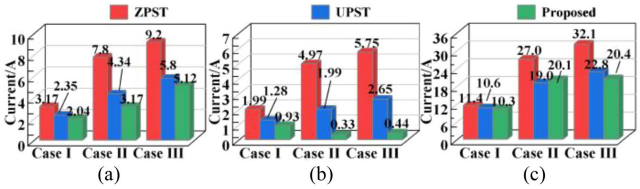


Fig. 17. Comparison of experimental data. (a) RMS value of TCRC. (b) RMS value of LFHC. (c) Peak to peak current of TCRC.

TABLE VIII
COMPARISON OF THE RIPPLE CURRENT OPTIMIZATION TECHNIQUES

| Method | Algorithm complexity | LFHC suppression performance | DC bias current | Applicability |
|---|---|---|---|---|
| UPST | **Low** | Medium | **No** | **Wide** |
| [25], [26] | Medium | / | Yes | Medium |
| **Proposed** | High | **Best** | **No** | **Wide** |

* The methods presented in [25] and [26] neglect to account for constraint of PSA adjustable range, whose unmodified application will generate serious dc bias current, thus precluding meaningful evaluation of its LFHC suppression performance in DAB 3P1S ac–dc converter.

where the phase relationships of inductor currents for all three 1P converters are explicitly annotated. A comparative analysis reveals that the proposed phase shift method dynamically adjusts inter-module phase relationships according to output operating conditions, thereby achieving optimal ripple suppression performance. Furthermore, when implementing the proposed method, the number of modules operating in TDCM is explicitly annotated at the top of Figs. 13(c), 14(c), and 15(c). This parameter is exclusively determined by the instantaneous voltage transfer ratio and instantaneous transfer power. Consequently, while maintaining constant output voltage and average output power, this value varies with grid phase angle. Based on the aforementioned experimental results, a more comprehensive comparison based on experimental phenomena is given in Table VIII.

Fig. 16 presents detailed current waveforms during sector transition across consecutive switching cycles. The "Transition stage" label specifically denotes the first switching cycle of sector switching. To circumvent the dc bias current induced in the inductor during phase adjustment, the dc bias suppression method proposed in [29] is implemented in this transition stage, thereby facilitating safe phase adjustment. However, while effectively eliminating dc bias current, this method induces elevated peak inductor currents during transient stage, as evidenced in Fig. 16(a). These current peaks, when processed by the secondary rectifier bridge, generate significant transient ripple current. Consequently, although the rms value of the TCRC is substantially reduced, the peak-to-peak ripple amplitude shows limited improvement compared to the UPST, as quantitatively demonstrated in Figs. 13–16 and 17(c).

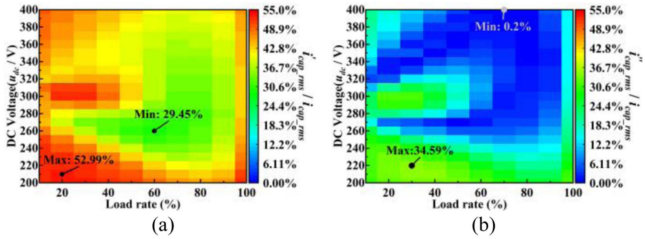


Fig. 18. Attenuation of the LFHC using different phase shift optimization methods under diverse operating conditions. (a) UPST (120° phase shift). (b) Proposed. ($i_{\rm cap\_rms}$: RMS value of the LFHC in the TCRC obtained using ZPST; $i'_{\rm cap\_rms}$: rms value of the LFHC in the TCRC obtained using UPST; $i''_{\rm cap\_rms}$: rms value of the LFHC in the TCRC obtained using the proposed method).

In addition, Fig. 18 demonstrates the ripple current elimination efficacy of the LFHC utilizing the UPST and the proposed method under varying output voltages and load rates. As demonstrated in Fig. 18(a), the UPST exhibits the optimal elimination effect at an output voltage of 260 V and a load rate of 60%, while the least effective result is observed at an output voltage of 210 V and a load rate of 20%. As demonstrated in Fig. 18(b), the proposed method exhibits its optimal suppression effect at a 70% load rate and a 400 V output voltage, while its least effective outcome is observed at a 30% load rate and a 220 V output voltage. The comparison group data indicates that

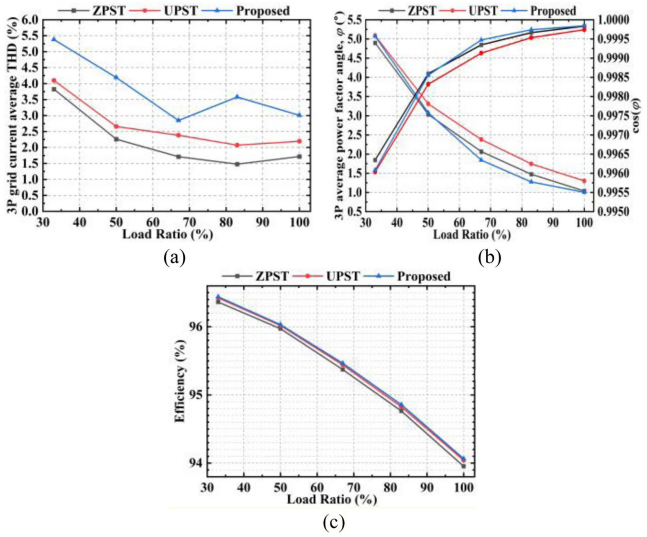


Fig. 19. Converter's technical specifications under three phase-shift configurations at 300 V output voltage. (a) THD. (b) Power factor. (c) Efficiency.

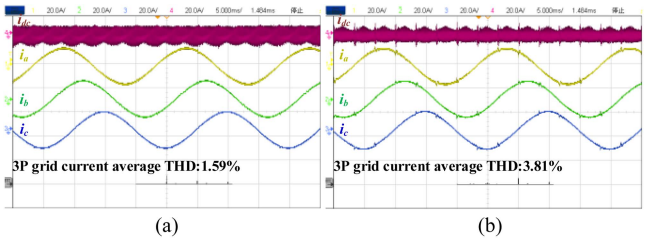


Fig. 20. Steady-state experimental current waveforms and DC-link capacitor ripple current spectrum, $u_{\rm dc} = 400$ V, $P_o = 3300$ W. ($i_{\rm dc}$—DC side ripple current, $i_a$, $i_b$, and $i_c$—the grid currents. (a) UPST (120° phase shift). (b) Proposed.

the latter exhibits a significantly superior optimization effect in comparison to the former.

Fig. 19(a) and (b) presents the grid current THD and power factor versus output power at an output voltage of 300 V. A comparative analysis of the three phase-shift techniques reveals that the proposed method exhibits approximately 2% higher THD, attributable to power transfer deviations during sector transitions which induce grid current distortion [31]. The occurrence of current dips or surges at the instants of sector transitions results in an augmentation of low-frequency harmonic components in the grid current, thereby leading to an increase in THD, as illustrated in Fig. 20(b). Nevertheless, THD maintains compliance with the conventional 5% threshold when the load ratio exceeds 40%. The efficiency curve of the converter is depicted in Fig. 19(c), illustrating that the efficiency of the converter is marginally enhanced with the proposed method. This can be ascribed to the fact that the proposed method reduces the rms value of TCRC. It is important to note that the proposed method does not alter the rms value of inductor current or the instantaneous current values at switching instants, except during the switching cycle of grid sector commutation. Consequently, the switching losses and conduction losses in power devices, as well as the losses of magnetic components, remain virtually unaffected by this method. However, the bus capacitor losses are a relatively small proportion of the total losses due to the high number of capacitors connected in parallel to the dc bus in the experimental prototype, resulting in a reduction of the total ESR. Consequently, the observed enhancement in efficiency is not substantial.

## V. Conclusion

The study introduces a dual phase-optimized strategy grounded in Fourier analysis. This technique aims to diminish the LFHC and consequently reduce the rms of the TCRC in the DAB-3P1S ac–dc converter. In contrast to the OPSA calculation method developed for nonisolated converters, this technique considers the limitations imposed on the adjustable range of PSA in DAB-based isolated converters. First, a computational method is proposed to determine the OPSA among three parallel DAB 1P1S ac–dc converters for a given adjustable range of PSA. Subsequently, an optimization algorithm is constructed based on this method to find the optimal initial phase relationship. The LFHC in the TCRC is substantially reduced using this dual phase-optimized strategy, which combines offline optimization and online calculation. The experimental results demonstrate the efficacy of the proposed method, achieving a 90% reduction in LFHC within the TCRC under rated operating conditions.

## References

[1] U. S. Department of Energy, "Energy storage grand challenge: Energy storage market report," U.S. Dept. of Energy, Washington, DC, USA, Tech. Rep. DOE/GO102020-5497, Dec. 2020.

[2] P. Ma and D. Sha, "A single-stage AC–DC converter based on semi dual-active-bridge with decoupled inductor current modulation strategy," *IEEE Trans. Power Electron.*, vol. 38, no. 8, pp. 10170–10182, Aug. 2023.

[3] L. Schrittwieser, M. Leibl, and J. W. Kolar, "99% Efficient isolated three-phase matrix-type DAB buck–Boost PFC rectifier," *IEEE Trans. Power Electron.*, vol. 35, no. 1, pp. 138–157, Jan. 2020.

[4] X. Li, F. Wu, G. Yang, and H. Liu, "Improved modulation strategy for single-phase isolated quasi-single-stage AC–DC converter to improve current characteristics," *IEEE Trans. Power Electron.*, vol. 35, no. 4, pp. 4296–4308, Apr. 2020.

[5] Y. Xu, Z. Wang, Y. Shen, Z. Zou, and M. Liserre, "A VSC-based isolated matrix-type AC/DC converter without bidirectional power switches," *IEEE Trans. Ind. Electron.*, vol. 70, no. 12, pp. 12442–12452, Dec. 2023.

[6] T. Chen, R. Yu, and A. Q. Huang, "Variable-switching-frequency single-stage bidirectional GaN AC–DC converter for the grid-tied battery energy storage system," *IEEE Trans. Ind. Electron.*, vol. 69, no. 11, pp. 10776–10786, Nov. 2022.

[7] J. Ma, R. Cheng, S. Wang, P. Wang, and T. Liu, "Decentralized control strategy for switching harmonic elimination of modularized input Parallel Output Series Dual Active bridge converter," *IEEE Trans. Power Electron.*, vol. 38, no. 9, pp. 10595–10599, Sep. 2023.

[8] F. Fang, H. Tian, and Y. Li, "An improved SVM strategy to reduce DC current ripple for AC–DC matrix converter," *IEEE Trans. Ind. Appl.*, vol. 57, no. 1, pp. 570–579, Jan./Feb. 2021.

[9] H. Ding, Q. Li, X. Guo, Y. Yang, and Z. Lu, "Optimal modulation strategy for current-source converter to reduce DC-link current ripple," *IEEE Trans. Ind. Electron.*, vol. 70, no. 10, pp. 10271–10281, Oct. 2023.

[10] X. Guo, Y. Yang, and X. Wang, "Optimal space vector modulation of current-source converter for DC-link current ripple reduction," *IEEE Trans. Ind. Electron.*, vol. 66, no. 3, pp. 1671–1680, Mar. 2019.

[11] L. Ming, W. Ding, P. C. Loh, and Z. Xin, "A direct carrier-based modulation scheme with full index range for DC-link current ripple mitigation of a current source converter," *IEEE Trans. Ind. Electron.*, vol. 69, no. 1, pp. 452–462, Jan. 2022.

[12] J. Song et al., "A modified space vector modulation for DC-side current ripple reduction in high-frequency link matrix converter," *IEEE Trans. Transp. Electrific.*, vol. 8, no. 4, pp. 4470–4481, Dec. 2022.

[13] A. Mallik and A. Khaligh, "Intermediate DC-link capacitor reduction in a two-stage cascaded AC/DC converter for more electric aircrafts," *IEEE Trans. Veh. Technol.*, vol. 67, no. 2, pp. 935–947, Feb. 2018.

[14] A. M. Alcaide, S. Guenter, J. I. Leon, G. Buticchi, S. Kouro, and L. G. Franquelo, "Common DC-link capacitor lifetime extension in modular DC/DC converters for electric vehicle fast chargers via variable-angle interleaved operation," *IEEE Trans. Ind. Electron.*, vol. 70, no. 11, pp. 10765–10774, Nov. 2023.

[15] A. Tcai, H. -U. Shin, and K. -B. Lee, "DC-link capacitor-current ripple reduction in DPWM-based back-to-back converters," *IEEE Trans. Ind. Electron.*, vol. 65, no. 3, pp. 1897–1907, Mar. 2018.

[16] C. Xue, L. Ding, and Y. Li, "Improved model predictive control with reduced DC-link capacitor RMS current for back-to-back converter-fed PMSM drives," *IEEE Trans. Ind. Electron.*, vol. 71, no. 1, pp. 194–203, Jan. 2024.

[17] H. Tong, Y. Ke, W. Yao, and W. Li, "DC-link capacitor current stress minimization strategy for paralleled three-phase voltage-source converters with interleaving," *IEEE Trans. Power Electron.*, vol. 39, no. 5, pp. 5320–5338, May 2024.

[18] C. Wang, T. Yang, H. Hussaini, Z. Huang, and S. Bozhko, "Power quality improvement using an active Power sharing scheme in more electric aircraft," *IEEE Trans. Ind. Electron.*, vol. 69, no. 4, pp. 3588–3598, Apr. 2022.

[19] C. Wang, T. Yang, P. Kulsangcharoen, and S. Bozhko, "An enhanced second carrier harmonic cancellation technique for dual-channel enhanced power generation centre applications in more-electric aircraft," *IEEE Trans. Ind. Electron.*, vol. 68, no. 7, pp. 5683–5692, Jul. 2021.

[20] C. Wang, T. Yang, X. Lang, and S. Bozhko, "An advanced switching harmonic cancellation method for a dual-generator power system in more-electric aircraft," *IEEE J. Emerg. Sel. Topics Power Electron.*, vol. 10, no. 6, pp. 7120–7132, Dec. 2022.

[21] B. Yao, Z. Tang, D. Kumar, H. Wang, and H. Wang, "Optimal modulation strategy for ripple current reduction of DC-link capacitor in multidrive systems," *IEEE Trans. Power Electron.*, vol. 38, no. 9, pp. 11474–11487, Sep. 2023.

[22] S. Baburajan et al., "Design of common DC-link capacitor in multiple-drive system based on reduced DC-link current harmonics modulation," *IEEE Trans. Power Electron.*, vol. 37, no. 8, pp. 9703–9717, Aug. 2022.

[23] J. Poon, B. Johnson, S. V. Dhople, and J. Rivas-Davila, "Decentralized carrier phase shifting for optimal harmonic minimization in asymmetric parallel-connected inverters," *IEEE Trans. Power Electron.*, vol. 36, no. 5, pp. 5915–5925, May 2021.

[24] D. Zhang, F. Wang, R. Burgos, R. Lai, and D. Boroyevich, "DC-link ripple current reduction for paralleled three-phase voltage-source converters with interleaving," *IEEE Trans. Power Electron.*, vol. 26, no. 6, pp. 1741–1753, Jun. 2011.

[25] M. Schuck and R. C. N. Pilawa-Podgurski, "Ripple minimization through harmonic elimination in asymmetric interleaved multiphase DC–DC converters," *IEEE Trans. Power Electron.*, vol. 30, no. 12, pp. 7202–7214, Dec. 2015.

[26] F. An et al., "Selective virtual synthetic vector embedding for full-range current harmonic suppression of the DC collector," *IEEE Trans. Power Electron.*, vol. 38, no. 2, pp. 2577–2588, Feb. 2023.

[27] Y. Liu, T. Yang, X. Hao, Y. Qi, and W. Li, "Second-carrier harmonic cancellation for a DC bus fed by multiple dual active bridges in more electric aircraft applications," *IEEE J. Emerg. Sel. Topics Power Electron.*, to be published, doi: 10.1109/JESTPE.2024.3523529.

[28] J. Hu, S. Cui, D. v. d. Hoff, and R. W. De Doncker, "Generic dynamic phase-shift control for bidirectional dual-active bridge converters," *IEEE Trans. Power Electron.*, vol. 36, no. 6, pp. 6197–6202, Jun. 2021.

[29] J. Zhang, D. Sha, and P. Ma, "A dual active bridge DC–DC-based single stage AC–DC converter with seamless mode transition and high power factor," *IEEE Trans. Ind. Electron.*, vol. 69, no. 2, pp. 1411–1421, Feb. 2022.

[30] D. Cittanti et al., "Analysis, design, and experimental assessment of a high power density ceramic DC-link capacitor for a 800 V 550 kVA electric vehicle drive inverter," *IEEE Trans. Ind. Appl.*, vol. 59, no. 6, pp. 7078–7091, Nov./Dec. 2023.

[31] N. Mo et al., "Modulation-independent initial current control of DAB-based single-stage AC–DC converter for DC bias elimination," *IEEE Trans. Power Electron.*, vol. 40, no. 1, pp. 406–421, Jan. 2025.